Faculty of Natural Science and Technology
Department of Physics

NTNU
Innovation and Creativity

MASTER'S THESIS FOR

STUD. TECHN. HEGE SJEGGESTAD BJØRNSEN

Thesis started:	02.12.2007
Thesis submitted:	06.29.2007

DISCIPLINE: PHYSICS

Norsk tittel:	*"Nanopartikkel Avsetning i Dråper av Leire-Vann Suspensjoner"*
English title:	*"Nanoparticle Deposition in Droplets of Clay-Water Suspensions"*

This work has been carried out at NTNU, under the supervision of Professor Jon Otto Fossum

---

Trondheim, June 29th 2007

Jon Otto Fossum

Responsible supervisor

Professor at Department of Physics

Abstract

The physics of fluids play an important role in many areas of science, and several applications and experiments are requiring an accurate prediction of the evolution of the size and shape of a droplet. Even though many applications are involving the drying of extended films rather than single droplets, the typical practical situation, never involves perfectly uniform, flat, nor infinite films. Thus one might expect some flow driven phenomena that are similar to the case of droplets, and it is therefore very important to understand the physical properties of a single droplet.

For this Thesis the evaporation of droplets on substrates that are both wetting and non-wetting were studied. The droplets had an initial volume of about 1 μl and contained either pure water or a laponite suspension. The radius and mass of the droplets were followed in time until they reached zero, and pictures were taken with the optical microscope and the AFM during the drying process and of the final residue respectively.

Pictures from the optical microscope clearly show how a foot forms around the outer edge of the droplet. After a while the foot is separated from the cap in the middle and it is growing on the expense of the cap. The formation of the cap and foot can also be seen in the graphs, where the commencement of the formation is leading to a halt in the decreasing radius. This can be seen as a plateau in the figures, before the radius starts decreasing again with a faster evaporation rate. It is also obvious from the pictures that there is some kind of ordering in the final edge stain. This ordering gives rise to birefringence when viewed through crossed polarisers.

The evaporation rates were also studied, and were found to be about 2×10^{-3} mgs^{-1}. We found the relation between the radius and time to be $R(t) = C_R(t_0 - t)^{\alpha_R}$, where the constant C_R and the exponent α_R are depending on the different substrates and suspensions. The volume was found to be related to the radius by $V = C_V R^{\alpha_V}$, where C_V and α_V again were dependent on the substrates and the content of laponite.

The conclusion is that the evaporation process is dependent of two main parameters: The deposition surface, and the concentration of the solution.

Preface

This Master's Thesis was written as the final part of the Master of Technology degree, within the Technical Physics Program at the Norwegian University of Science and Technology, and is a continuation of the project work of fall 2006. The work was conducted over a period of 20 weeks in the spring semester of 2007, and I worked under the supervision of Professor Jon Otto Fossum and Doctor Ahmed Gmira.

The idea of this Thesis has been to investigate the behaviour of evaporating droplets of different suspensions deposited on different substrates. This was done utilising an optical microscope, and an Atomic Force Microscope, AFM, in contact mode.

I would like to thank Professor Jon Otto Fossum for welcoming me into the Complex group, and for letting me work with this exciting topic. I would also like to thank Doctor Ahmed Gmira for his contributions to this Thesis, by helping me analysing the data and assisting me with the AFM. At last I will thank Jon Sætrom for helpful advice regarding the mathematical aspects and feedback during the process.

Trondheim, June 29th 2007 Hege Sjeggestad Bjørnsen

Contents

1 Introduction

The formation of edge stains after suspension droplets have evaporated, is receiving increased attention not only due to the importance from a fundamental point of view, but also because of the relevance in different scientific and industrial applications [62].

In this Thesis we consider the situations of droplet evaporation on hydrophilic and hydrophobic glass surfaces. The droplets contain different concentrations of laponite, and their different behaviours are investigated. The build up of colloidal particles at the edge of the drying droplets, is leading to a crusting of the free surface, which again leads to a separation into an outer and inner part of the droplets. Towards the end of the evaporation, a deposit similar to a coffee-stain can be seen. As the drop is evaporating, the solvent is flowing toward the contact line, carrying suspended particles with it. As all the solvent has evaporated, a ring formed residue of particles is left on the substrate. For this to happen the contact line of the evaporating droplets has to be pinned by the roughness of the substrate, and later by the deposit of particles here [35]. The Marangoni effect is counteracting this coffee-stain effect, by depositing the particles in the centre rather than around on the edge of the droplet [23].

If thermal and Marangoni effects are neglected, the evaporation rate is proportional to the perimeter of the droplet $\mathrm{d}V/\mathrm{d}t \propto -2\pi R$, where t is the time, V is the volume, and R is the radius of the droplet [14, 42]. With an ellipsoidal shape, the volume is proportional to $R^2 h$, where h is the height. By considering that the contact angle is constant, it follows by integration that $R \propto (t_0 - t)^{1/2}$, where t_0 is the time at which the droplet vanishes. This behaviour is expected where the evaporation is purely diffusive, and has earlier been found for organic liquids. Bonn et al. [42] found that the mass of a water droplet, and consequently the volume, is not proportional to R^3 but to $R^{2.3}$, and that the height decreases much more slowly than the radius.

Instead of being proportional to $(t_0 - t)^{1/2}$, we found that R was related to $t_0 - t$ by $R = C_R (t_0 - t)^{\alpha_R}$, where C_R and α_R turned out to be considerably smaller than the results found by Bonn et al. [42] ($C_R \sim 0.13$ and $\alpha_R \sim 0.3$). The relation between the evaporating droplets' volume and radius were also calculated to be quite different than what has earlier been found, with the closest match for the water droplet on hydrophilic glass, with $V \propto R^{1.5}$.

The theoretical part of the Thesis starts off describing the physics of droplets and some basic information about clay and laponite. Then there is a presentation of the equipment that have been used during the experiments together with some general information on optics and particle orientation. In Section 8, the actual equipment is introduced, before the experimental methods are described. The results from the experiments are presented in Section 9 together with an explanation to the phenomena. There is also an evaluation of the possible error sources.

2 The Physics of Droplets

The physics of fluids is playing an important role in many areas of science. For the past few years there has been a lot of research concentrated on micro-scale flows, where the usual laws of hydrodynamics break down [50]. The hydrodynamical laws are no longer valid because the continuum theory only considers macroscopic quantities [25].

The basic entity of a microfluidic system is the droplet. Understanding the physical properties of a single droplet is very important, as several applications and experiments require an accurate prediction of the evolution of the size and shape of a droplet. In many applications one also needs to be able to control these parameters. The influence of surface tension, of the viscosity of the liquid, the interaction of the droplet with the substrate and the impact of a droplet on a solid are all examples of the many experiments that can give interesting information of the physics of droplets. The complexity of such systems comes down to the competition between surface effects and bulk properties [50].

There has lately been attracted a great deal of attention to the seemingly simple problem of evaporating droplets. The two situations that have been studied most are droplets deposited on a rough[1] substrate where the contact line remains pinned during the evaporation, and droplets of completely wetting liquids deposited on a perfectly smooth and wetting surface where no anchoring of the contact line occurs [42]. In this Thesis the focus will be on the first case, where two main effects take part in the evaporation process of the droplet:
The first is the "coffee-stain effect", where virtually all the solute may end up on the edge. The second is temperature-gradient-induced "Marangoni-Bénard convection", which results in irregular patterns due to an upward flow of the warmer lower liquid [61].

2.1 Crusting

During solvent evaporation, there is a local increase in the concentration of the particles at the vapour/drop interface. This accumulation of particles may lead to the formation of a glassy skin or crust which is slowing down the evaporation, without blocking it totally. The solvent is still able to diffuse through the glassy layer. The surface area remains constant but it is bending as the volume of liquid it encloses decreases [39, 17]. This is seen in Figure 1.

We often get the formation of an outer "foot", and a central "cap" in evaporating droplets. The foot is a dense colloidal solid, and while the cap is depositing

---

[1] The roughness of a surface is a measure of its lack of order [48]. The Illustrated Oxford Dictionary explains the word rough as "Having an uneven or irregular surface, not smooth or level or polished" [32]. If the surface contains a single prominence, it would not have been referred to as rough; if it contains a few it might have, and if there were several prominences, we would certainly refer to it as rough. In other words, roughness is a property which is easy to define, but whose value depends on the technique or scale of measurement [48].

particles into it, the particle concentration here is increasing. The particle concentration in the cap does therefore not increase as the solvent is evaporating. The foot is also advancing by the slow deposition of colloidal particles at the foot-cap border, while the radius of the cap decreases [21, 37]. The final residue will often have a dense, almost opaque foot around the outside of the drop, and only a thin layer of colloid in the centre. The initial composition of the droplet will, however, decide the colloidal structure and flow behaviour inside the foot and cap [21].

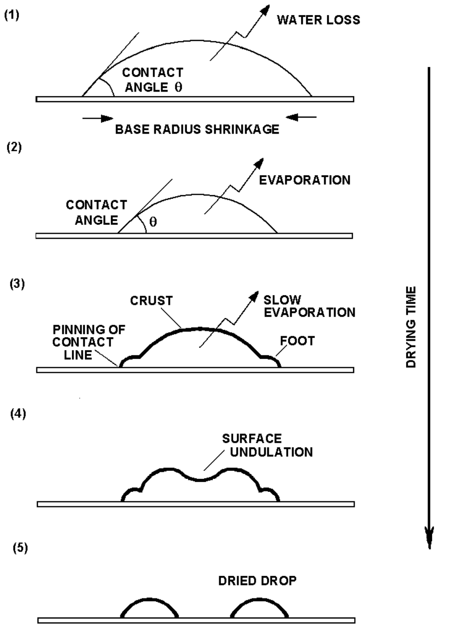

Figure 1: **Schematic of the drying process:** The drop maintains a fixed contact angle as the base radius shrinks. The contact line is pinned, and crust is formed at the free surface which is slowing down the evaporation rate. A foot is also appearing on the same time. As the evaporation continues, the volume beneath the crust is decreasing, and a surface undulation appears because of the constant surface area. When all the solute has evaporated, the crust is sitting in the laponite deposit [17].

2.2 The Coffee-Stain Effect

The ring shaped residue left when a spilled drop of coffee evaporates on a solid surface, is usually darkest, and thus most concentrated, along the perimeter, which is illustrated in Figure 2. The coffee, which initially was dispersed over the entire droplet, now becomes concentrated into a tiny fraction of it [14]. This ring formation is due to a hydrodynamic process, called the coffee-stain effect, where solids (coffee powder) dispersed in the drop are advected to the contact line [13]. The ring-like stains are not particular to coffee but a general phenomenon for any sessile droplet containing solid constituents [15, 62]. The effect will not be present in a droplet of pure solvent, like water, as there are no particles to pin the perimeter of the drop [21].

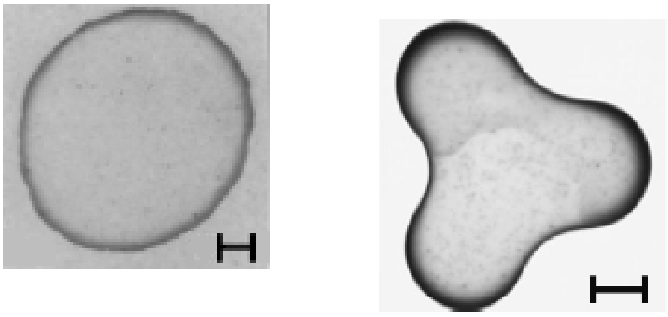

(a) (b)

Figure 2: (a) Normal ring shaped coffee-stain. (b) Manipulated coffee-stain which is darkest at the extremities because of a larger evaporation surface [15].

Two main mechanisms are responsible for the coffee-stain effect: Contact line pinning and predominant evaporation at the edge of the droplet [15]. Because the evaporation rate in a pinned drop is greatest at the edge, the evaporated liquid has to be replenished by a convective flow of liquid from the interior to maintain an equilibrium droplet shape with a fixed boundary. The resulting outward flow may transfer 100% of the solute to the edge, see Figure 3 [15, 43].

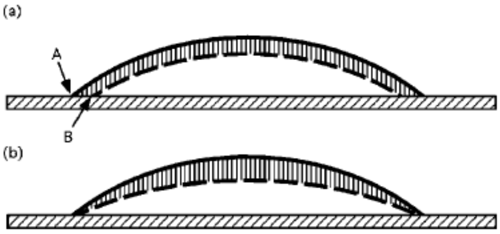

Figure 3: Origin of the advective current. (a) Uniform evaporation. Without a pinned contact line the interface is moving from the solid line to the dashed line, and the contact line from A to B. (b) Non-uniform evaporation. The movement of the contact line is prevented by pinning, and a resulting outward flow is replenishing the evaporated liquid [15].

The drop is also self-pinning, which means that the initial roughness or chemical heterogeneities of the substrate are providing a foothold where the contact line first sticks. As there is an accumulation of material at the edge, the pinning is strengthened, and eventually this takes over as the primary source of pinning [15, 49].

2.3 The Marangoni Effect

Hu and Larson [23] show that the formation of coffee-stain like deposits not only requires a pinned contact line, but also suppression of the so called Marangoni flow. For interfaces clean of surfactants, the Marangoni flow reverses the coffee-stain phenomenon and produces deposition at the droplet centre rather than the edge.

Since the pioneering studies of Thomson, Marangoni and Bénard in the late 19th century, there has been a lot of attention devoted to what are known as Marangoni instabilities [46]. These instabilities are caused by the non-uniform cooling at the surface as the solvent is evaporating. The small perturbations in the surface temperature are in turn leading to a surface tension gradient, which decreases with rising temperature [23, 35].

The lowest temperature can be found at the top of the liquid-air surface, due to a longer thermal conduction path, and because the surface tension is highest there. This is inducing a radially inward Marangoni flow near the droplet surface. Further particles that are near the free liquid surface of the droplet are carried from the edge towards the top of the droplet, and then plunged downward to adsorb onto the substrate, or to be carried along the substrate back to the edge. This is seen in Figure 4. At the edge the particles are recirculated along the free surface back toward the top of the droplet [23]. In other words, the Marangoni effect is *flows driven by surface tension gradients, if the temperature within the droplet is nonuniform* [42]. The effect is, however, weak for water droplets [23].

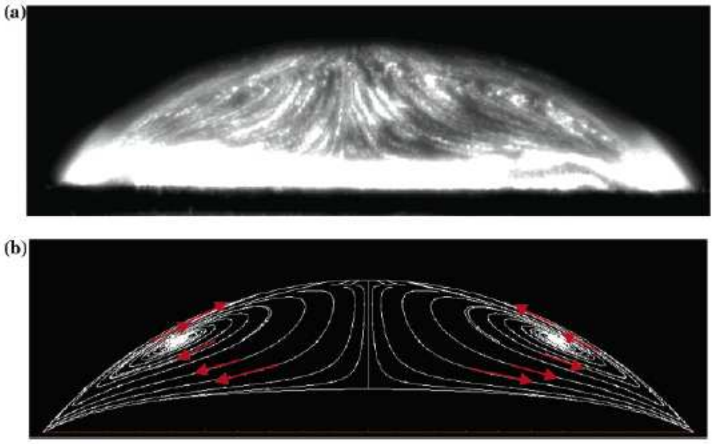

Figure 4: The flow field in an evaporating octane droplet, (a) experimentally and (b) predicted [23].

3 Clay

Clay was among the first materials utilised by man, and has been known to, and used by, humans for thousands of years. Archaeologists have found artifacts dating back to approximately 23,000 BC [5, 24]. The scientific study and resulting applications beyond traditional approaches, however, is a relatively recent discipline, which only has roots back to the mid-1930s [5, 19].

There has been a growing scientific activity in the science of clay with the availability of clean chemistry customised synthetic clays [18, 19]. This multidisciplinary approach is at the border between materials science and colloid science, while the multi-scale approach, which is linking nano-, micro- and macro-scale studies, is a challenge for the future of clay science. As clays and clay materials are abundant, inexpensive and environmentally friendly, they will most likely be known as the materials of the 21st century [5].

Clay minerals are a group of phyllosilicates, a subgroup of the silicates [2, 27, 38]. The particles are platelet shaped, with ∼ 1 nm thickness, and a lateral size which varies between a few tenths of nanometers up to a few micron [18, 38]. Clays are characterised by a layered structure, where the "unit cell" or layer of clay platelets is made of the connection between tetrahedral and octahedral sheets in three dimensions, as can be seen in Figure 5 [38]. The different layers are held together by van der Waal's forces [24].

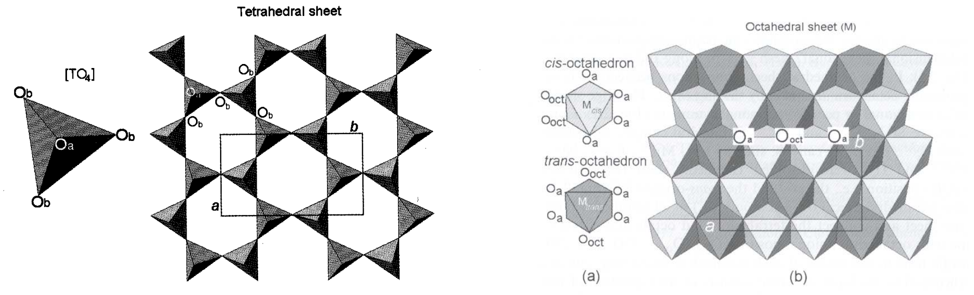

(a) (b)

Figure 5: (a) The tetrahedral sheet is made up of tetrahedra. (b) The octahedral sheet is made up of octahedra. O_a and O_b are referring to the apical and basal oxygen atoms, respectively, while *a* and *b* refer to the unit-cell parameters [5].

The continuous two-dimensional tetrahedral sheets consist of e.g. SiO_4, AlO_4 or FeO_4, four oxygen atoms at the corners, and a cation in the middle. The octahedral sheets are made up of octahedra formed from small cations, such as Al^{3+}, Fe^{3+}, Mg^{2+} or Fe^{2+}, coordinated by six oxygen atoms [2, 5, 38].

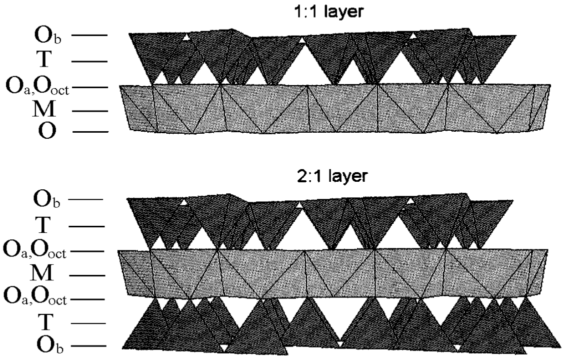

Figure 6: 1:1 and 2:1 layer structure. O_a, O_b and O_{oct} are referring to the tetrahedral apical, tetrahedral basal and the octahedral anionic position, respectively. M and T are the octahedral and tetrahedral cations, respectively [5].

Clays are categorised depending on how the tetrahedral and octahedral sheets make up layers: The 1:1 layer structure consists of the repetition of one tetrahedral and one octahedral sheet in each layer. The unit cell is made up of four tetrahedral sites, and six octahedral sites. The 2:1 layer structure, on the other hand, consists of one octahedral sheet sandwiched between two tetrahedral sheets. Here eight tetrahedral- and six octahedral sites make up the unit cell [5, 38]. The layers can have no charge, or a net negative charge depending on the composition of the tetrahedral and octahedral sheets. In the case of a charged layer, the charge is balanced by interlayer cations like Na^+ or K^+ [60]. The 1:1 and 2:1 layer structures are pictured in Figure 6.

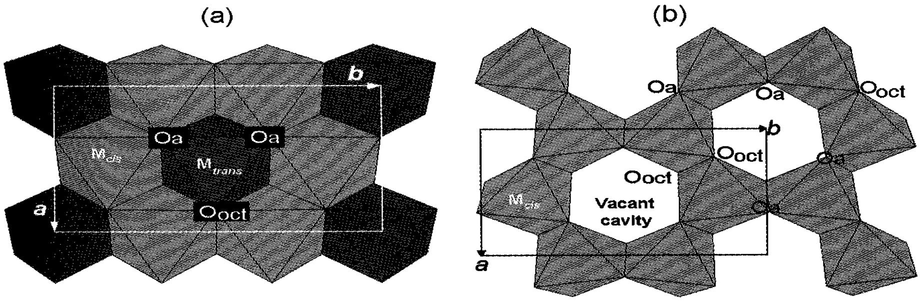

Figure 7: (a) Trioctahedral sheet and (b) dioctahedral sheet. O_a are the apical oxygen atoms shared with tetrahedra, while O_{oct} is the anionic site that is shared between neighbouring octahedra. *a* and *b* are the parameters of the unit cell [5].

2:1 clay minerals are referred to as dioctahedral when four of the six octahedral sites in the unit cell are occupied by cations, while the trioctahedral minerals are those with all six octahedra occupied [5, 38]. This is illustrated in Figure 7.

3.1 Smectites

Smectite clay is a generic name for a 2:1 phyllosilicate, with particles made up of stacks of clay platelets with intercalated balancing cations. The charge density is relatively moderate compared to other 2:1 clay minerals, and is varying between 0.4 e^- and 1.2 e^- per unit cell [5, 38]. A moderate surface charge, like this, is allowing the exchange of intercalated cations with other cations. This charge is allowing penetration of water- or other polar molecules in the interlayer space between the platelets which is causing the smectite grains to swell [38].

3.2 Laponite

Laponite, a synthetic 2:1 trioctahedral hectorite swelling clay, is the most widely studied synthetic clay until now [3, 19]. Its layers are composed of two tetrahedral silica sheets with an octahedral magnesia sheet in between, as seen in Figure 8. The chemical composition of laponite is $Si_8Mg_{5.45}Li_{0,4}H_4O_{24}Na_{0,7}$ [3].

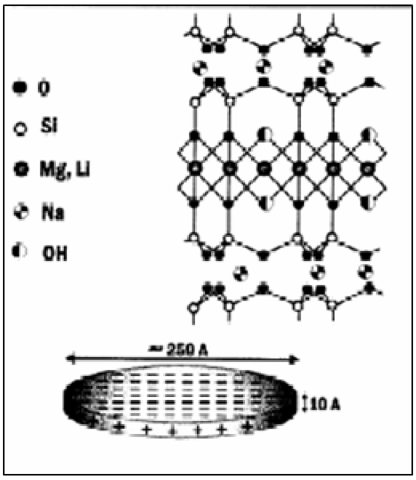

Figure 8: The laponite structure [10].

Laponite is an interesting clay model system because of its monodispersity and the small particle diameter of about 25 nm. In contrast, natural and other synthetic clays are in general polydisperse with a diameter of a few microns. With a thickness of only 1 nm, the platelets may individually be thought of as single crystals (see Figure 9) [10, 18, 19]. The laponite particles have a structural negative charge. This charge is balanced by Na^+ counter ions, which are located around the particles [3].

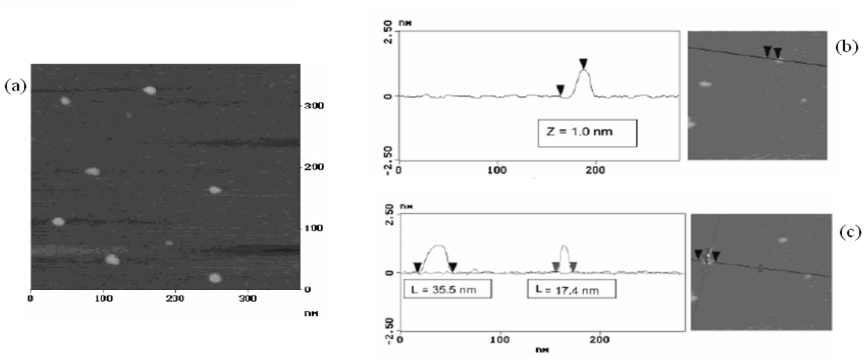

Figure 9: Laponite particles imaged with an atomic force microscope. (a) Isolated laponite particles. The thickness of the laponite particle (b) is 1 nm, and the diameter (c) is between 17 and 36 nm [3].

The two most common ways to utilise laponite are: As a rheology modifier, added to the formulation of products like surface coatings, household cleaners, personal care products and other water borne products. It can also be used as a film former, to produce electrically conductive, antistatic and barrier coatings.

There are four fundamental phases, identified experimentally, that govern the overall behaviour at relatively low particle concentrations in the phase diagram of laponite:

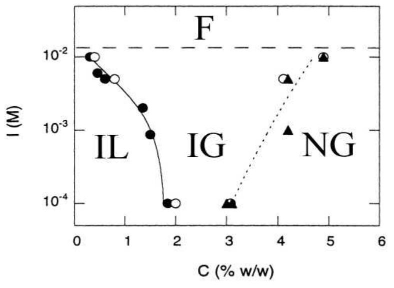

Figure 10: Phase diagram of laponite, where C is the concentration of laponite in units of weight percent in water and NaCl, and I is the concentration of NaCl in units of mol/l [33].

First an isotropic liquid (IL) phase which consists of suspended aggregates of primary clay particles. Then, an isotropic gel (IG) phase is observed, where percolating aggregation with fractal properties both dependent on salt-clay concentration and on time. Third, a nematic gel (NG) phase occur, for which excluded volume particle alignment has been proposed. There is also a flocculated

(F) phase at high electrolyte concentrations [18, 19]. The different phases in the phase diagram are illustrated in Figure 10.

3.3 Applications

When mixed with limited amounts of water, clays become plastic and are then easy to shape. As the clay dries, it becomes firm, and will retain this shape. When clay is exposed to temperatures above 500°C, irreversible chemical reactions begin to take place which makes it hard and water-resistant [24]. These properties are making clays ideal substances for producing durable pottery items. With different clay types and different drying conditions, clay has become absolutely necessary to our modern lives. It is the material of different kinds of ceramics, such as earthenware, bricks, porcelain and sanitary ware. Clays can also be used in many industrial processes which include cement production, chemical filtering, oil well drilling and construction, and one can find it in paper, plastics, paints, rubber and cosmetics. In addition it has a great importance to crop production, as clays are an important component of soils [5, 19, 27].

4 Microscope

When viewing objects that are too small to be seen by the naked or unaided eye, a microscope is utilised to give us a large image of the tiny object [56]. The size of the retinal image of an object decides its apparent size, and the most favourable distance for a normal eye at which to examine the detail of any object, is about 25 cm. This means that 25 cm is the least distance of distinct vision. If then a convergent lens is placed between the eye and the object, the object may be brought much closer. The lens will then form an enlarged virtual image at a distance which is greater than the object itself [9].

By the use of a microscope it is possible to recognise, interpret and manipulate objects which were unknown before the microscope and therefore not possible to influence. Consequently microscopy has played, and still plays an important role in the discovery of the world around us. The microscope is primarily a visual instrument, which produces images to be observed by the human eye, but images can also be recorded by photographic- or video-cameras, adapted to the visual instrument [6].

4.1 History

The origin of the microscope is uncertain, as many people contributed to its early development [31]. The first microscopes trace their history back about 400 years, and the first useful microscope may have been developed in the Netherlands as early as in 1590. Its inventor was the Dutch spectacle maker Zacharias Janssen (ca.1580-ca.1638) of Middleburg, probably with the help of his father Hans Janssen. Galileo (1564-1642) was announcing his invention of a compound microscope twenty years later [22]. Hooke (1635-1703) played the great part in the further development of the compound microscope, and future trends in design are actually somewhat present in some of his instruments, as can be seen in Figure 11. New ways of using the compound microscope are still being found and it is continuously being further developed [31].

4.2 The Optical Microscope

There are many different microscope designs, and they can largely be separated into two classes: optical theory microscopes and scanning probe microscopes. Optical theory microscopes function through the optical theory of lenses, and magnifies the image generated by the passage of a wave through the sample. The waves used can be either electromagnetic (optical microscopes) or electron beams (electron microscopes). The optical microscope contains one or more lenses producing an enlarged image of an object which is placed in the focal plane of the lens(es). Because of their use of visible wavelengths of light, the optical microscopes are the simplest and thus most widely used type of microscope. Even simple microscopes, with a single small lens, gave amazingly clear images to the earliest microscopists [56].

Figure 11: A sketch of one of Hookes microscopes from 1665, lit up by a candle [31].

4.3 The Compound Microscope

The compound microscope is made up of three main parts: the objective, the eyepiece and the tube or body. The objective, which is the lens or mirror that receives the first light rays from the object being observed, provides a magnified image of the object. This image is magnified further by the action of the eyepiece and eye together. The body is keeping all the different parts together and also keeps ambient light excluded [8]. Compound microscopes, often with a series of lenses, are today serving uses in many fields of science [56].

4.4 How a Microscope Works

The parts of the microscope and their relationship with each other are shown in Figure 12. The objective lens can be described as a lens with a very short focal length. It forms a real, inverted, and usually magnified image of the object which resides at the field stop or focal plane of the eyepiece [22, 8, 31]. The rays that diverge from each point of this image will emerge from the eyepiece lens parallel to each other [22]. The eyepiece lens is magnifying the image further, and places the image of the object at infinity for relaxed viewing by the eye [8].

The magnification of a compound microscope is the product of the transverse linear magnification of the objective, M_{To}, and the angular magnification of the eyepiece, M_{Ae} [8, 22, 44],

$$\mathrm{MP} = M_{To} M_{Ae}. \tag{1}$$

Thus, a microscope with a 2× objective used with a 10× eyepiece lens will provide a magnification of 20×.

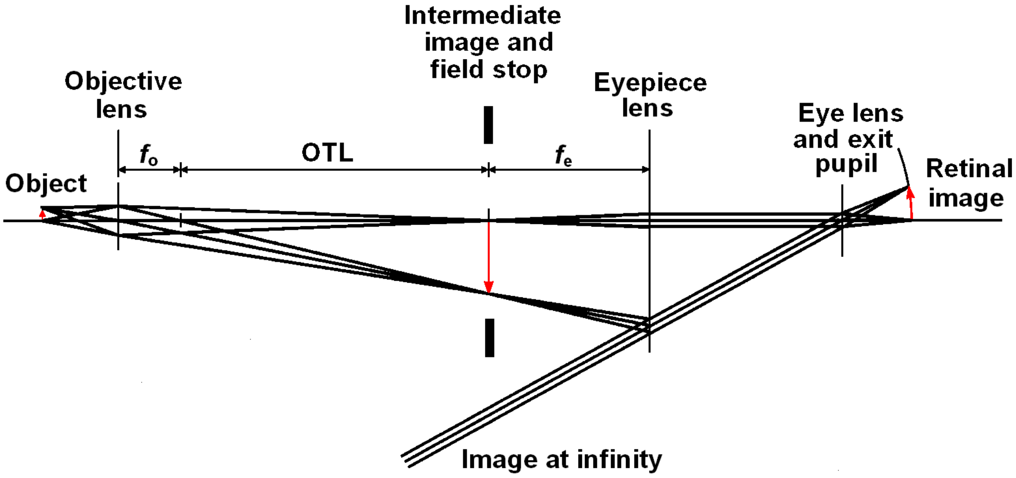

Figure 12: The object, just outside the focal plane of the objective, is imaged onto the retina through a system of lenses [8].

Because the optical microscope is using visible light, the limit of resolution is about 200 nm. This is the physical limit imposed by the wavelength of light, which means that the microscope will not be able to produce the image of objects smaller than the length of the light wave [47].

5 Light Birefringence and Particle Orientation

5.1 Polarisation

An electromagnetic wave can be resolved into two components, travelling at the same velocity, at 90° to each other. Light is usually unpolarised, with equal amounts of energy in the two polarisations, but under certain circumstances randomly polarised light can become plane or linearly polarised [8].

An ideal polariser is producing linearly polarised light from unpolarised light. When two ideal polarisers are aligned such that their transmission directions are placed at an angle θ, the vector component perpendicular to its transmission plane is absorbed. The reduced amplitude is given by *The Law of Malus*, $E = E_0 \cos\theta$. The transmitted intensity is proportional to the square of the amplitude, and the intensity is thus given by: $I = I_0 \cos^2\theta$. For crossed polarisers, with $\theta = 90°$, the intensity is zero, and all light is eliminated. Even though crossed polarisers block all light, putting a third polariser at 45° between them result in some transmission of light [26].

5.2 Refraction

When light travels from a medium with a given refractive index to a medium with another, refraction will occur as seen in Figure 13. The phase velocity of the wave is altered at the boundary between the two media. The wave will also change its direction and the wavelength will increase or decrease. The frequency, however, will remain constant. Refraction can either be sudden or gentle depending on how sudden the change of refractive index [8].

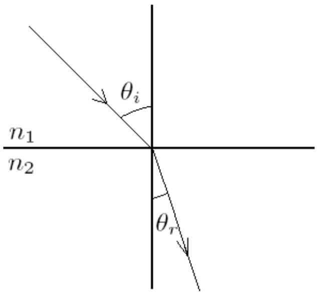

Figure 13: When light is travelling between two different media with different refractive index, the ray is refracted.

5.3 Birefringence

Many crystalline substances (i.e., solids whose atoms are arranged in some sort of regular repetitive array) are optically anisotropic. In other words, their optical properties are not the same in all directions within any given sample. [22]

While light will travel through isotropic materials at the same velocity regardless of their orientation, anisotropic materials have double refraction or birefringence: When a ray of light is traversing such a material, it is separated into two rays at a slight angle to each other (the ordinary ray and the extraordinary ray). In an anisotropic material, the light that at the materials surface obey Snell's law[2] is called the "ordinary" rays. These rays will experience a given refractive index and behave according to the laws of refraction and reflection. The rays that do not always obey Snell's law, on the other hand, are the "extraordinary" rays. These rays will, according to its direction and wavelength, experience a completely different value of refractive index [8]. This occurs when the ray passes through certain types of material having two different indices of refraction. The two beams are linearly polarised, and their polarisation states are orthogonal, as seen in Figure 14 [55, 9, 8].

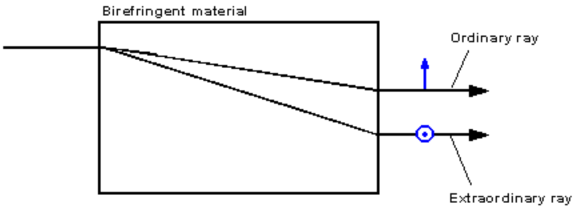

Figure 14: When light is travelling through a medium with different refractive indices, we get double refraction or birefringence.

The birefringent properties of materials may be described in terms of the anisotropic electrical properties of molecules of which the materials are composed. Birefringence may, however, arise from anisotropy on a scale much larger than molecular, namely when there is an ordered arrangement of similar particles of optically isotropic material whose size is large compared with the dimensions of the molecules, but small compared with the wavelength of light. We then speak of form birefringence [9].

---

[2] Snell's law is the formula that allows us to calculate the angle of refraction at a refractive index boundary:

$$n_1 \sin\theta_i = n_2 \sin\theta_r, \tag{2}$$

where θ_i is the angle of incidence in a material with a refractive index n_1, and θ_r is the angle of refraction in a material with the index n_2 [8].

5.4 Nematic Phase

Liquids are always isotropic, which means that they are not orientation dependent. The reason for this is the lack of preferred orientation in the thermal motion. For a special class of molecules, a macroscopic anisotropy arises due to a spontaneously developing inner ordering in the liquid phase. The anisotropic state which they form is referred to as nematic, and the molecules are called nematogens. A common feature of most of the molecules which form this kind of anisotropic liquid phase, is that they have a rod-like form.

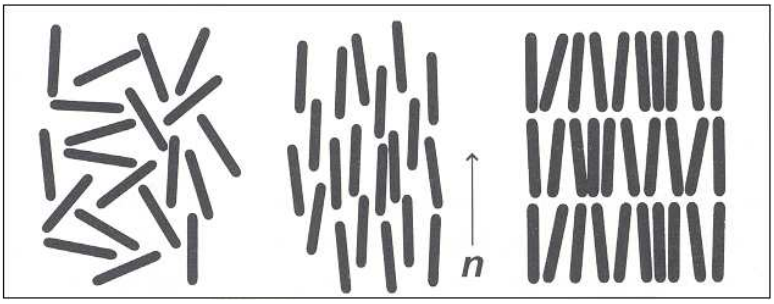

Figure 15: The three phases of a liquid-crystalline substance, the isotropic (left), nematic (middle), and smectic (right) [45].

In Figure 15, the sketch in the middle is illustrating the microscopic structure of the nematic phase, where the centres of gravity of the molecules are arranged as in a liquid. There is, however, no isotropic distribution of the orientation of the molecular axes for the nematic phase, with a well-defined preferred overall orientation. The preferred direction is not constant over the whole sample, but is slowly changing over macroscopic length-scales of μm. A unit vector (denoted by $\boldsymbol{n}$ in the figure) is specifying the preferred orientation. This unit vector is referred to as the nematic director and it determines the direction of the optical axis [45].

6 AFM

The Atomic Force Microscope (AFM) was invented in 1986 by Binnig, Quate and Gerber, and it is today one of the leading tools of imaging, measuring and manipulating matter at nanoscale [58]. It is a type of Scanning Probe Microscopy (SPM), which makes use of the small forces that can be found between materials in close proximity to the surface. AFM can therefore be applied to all kinds of materials, conducting, semiconducting and insulating [41].

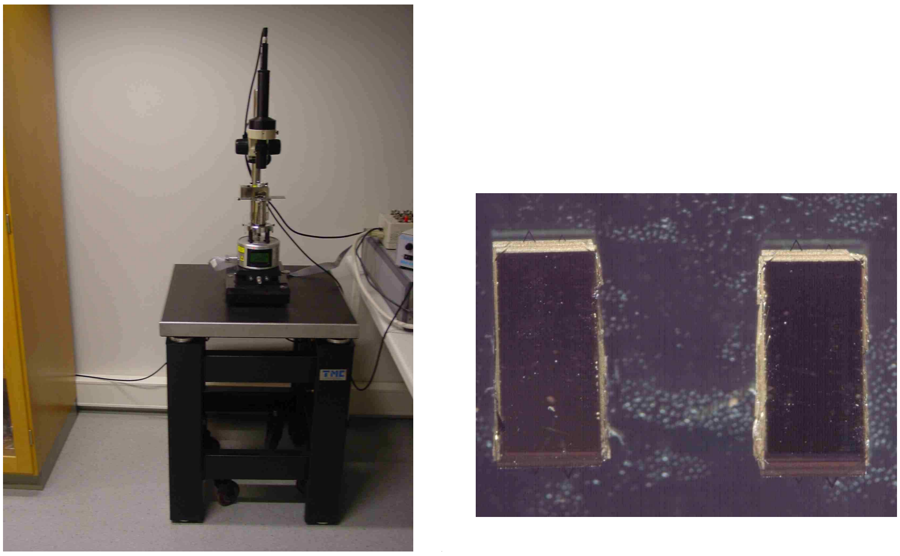

(a) (b)

Figure 16: (a) The MultiMode^{TM} Atomic Force Microscope on top of a vibration insulator. (b) Silicon nitride cantilever probes used for contact mode AFM.

The AFM is utilising a micro scale cantilever, usually made of silicon or silicon nitride (see Figure 16), with a sharp tip at its end that is scanning the surface of the sample. The tip is placed very close to the surface, and attractive and repulsive forces between tip and sample are leading to a deflection of the cantilever [58]. The deflection is measured by a laser spot reflected from the top of the cantilever into a position-sensitive detector that is made up of two side-by-side photodiodes. The difference between the signals from the two photodiodes is indicating the position of the laser spot on the detector, and thus the angular deflection of the cantilever [4]. This is shown in Figure 17. The AFM pictures can be presented by means of either height, deflection or friction.

To maintain a contact force, a feedback mechanism is adjusting the distance between tip and surface. For this purpose the sample is mounted on a piezoelectric tube, which can move the sample in the z-direction. It also moves in the x- and y-directions, and the result is a map of $s(x, y)$ which is representing the topography of the sample [58].

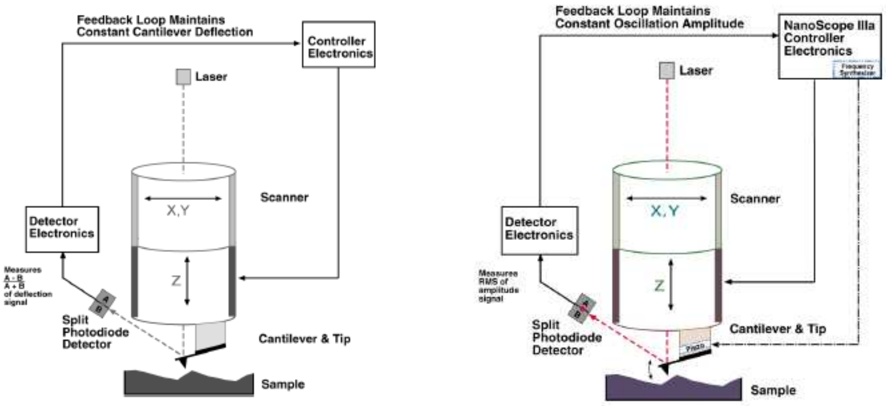

(a) (b)

Figure 17: (a) The feedback loop is maintaining constant cantilever deflection in Contact Mode. (b) Feedback loop electronics in Tapping Mode [52].

There are primary two modes of Atomic Force Microscopy: contact mode and tapping mode. In contact mode the cantilever tip is scanned across the sample surface while the tip is in actual contact with the surface. The change in cantilever deflection is monitored, and thus the surface topology is mapped. The accuracy of the scanning corresponds to the sharpness of the tip [41]. In tapping mode the probe is carefully oscillating in the z-direction, tapping the surface and thus detecting the surface hardness [41]. The cantilever is oscillating in free air at its resonance frequency. As the cantilever is bouncing vertically, the reflected laser beam is deflected in a regular pattern over a photodiode array, generating a sinusoidal electronic signal [16].

6.1 Resolution

As traditional microscopes use optical lenses they only have one measure of resolution, the resolution in the plane of the image. The resolution of the AFM is limited by the shape of the probe, rather than diffraction effects, and thus has two measures of resolution, the plane of the measurement (lateral(x, y)), and in the direction perpendicular to the surface (vertical(z)). Atomic force microscopy thus becomes a three dimensional imaging technique [4, 34].

Lateral resolution is usually defined as the ability to distinguish two separate points on an image [30]. This resolution depends on the geometry of the probe that is used for scanning. The radius of curvature of the end of the tip is determining the highest lateral resolution that can be obtained with a specific tip. A sharper tip with a small radius of curvature can thus laterally resolve smaller features than a dull tip with a larger radius of curvature, (see Figure

18) [52]. The sharpest tips available commercially can have a radius as small as 50 Å [7]. The sidewall angles of the tip is also determining the ability to probe a high aspect ratio. In addition it is possible, in the software, to choose the number of data points (pixels) present in the image in the x and y direction. It is not possible to resolve features smaller than the pixel size of the image [52].

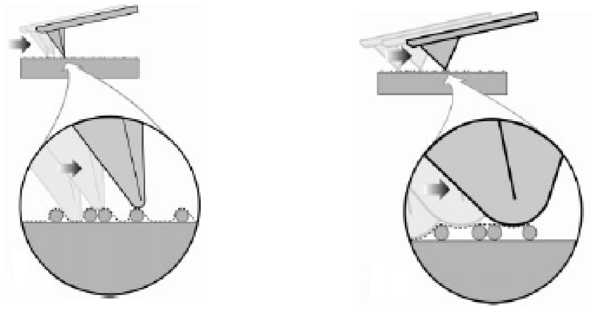

(a) (b)

Figure 18: Surface scanned with (a) a sharp tip and (b) a dull tip. The smaller the radius of curvature, the smaller the resolved features. A sharper tip can laterally resolve smaller features than a dull tip [52].

The resolution in the vertical direction is not determined by the tip shape. Instead it is primarily determined by the resolution of the vertical scanner movement, which is <1 Å. The sidewall angles of the tip determine the AFM's ability to image steep sidewalls on a sample surface, which means that the tip is not able to profile sides of surfaces steeper than the sidewall angle of the tip. This implies that the sidewall angle in the images will reflect the sidewall angle of the tip when scanning across features which are steeper than the tip, as seen in Figure 19. The size of the smallest resolvable height change is limited by the

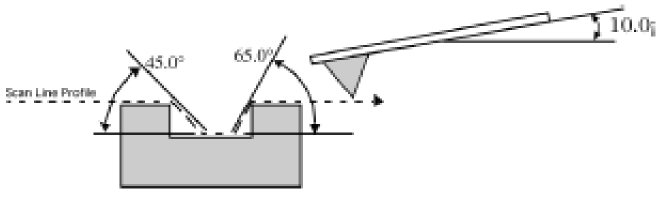

Figure 19: Scanning of features that are steeper than sidewall angle of the tip, the sidewall angle in the image will reflect the sidewall angle of the tip. (Scanning angle from front to back, i.e. scan angle = 0°) [52].

number of pixels in the vertical direction [52].

The overall system noise is the largest factor limiting the vertical resolution that can be acquired with the AFM. This may be a result of combined effects from acoustic noise, floor vibrations and thermal vibrations. To get the maximum vertical resolution the vibrations need to be minimised [34]. The AFM is thus placed on a vibration isolator in a room of constant temperature, as seen in Figure 16(a) [52]. The AFM can achieve a resolution of 10 pm, and unlike electron microscopes it can image samples in different environments, such as liquids, vacuum and low temperatures [4].

7 Thermogravimetric analysis

For an experiment it might often be interesting to know the mass of the investigated sample, and the measurement of mass is often one of the first quantitative experiments to be performed. Extending this technique into analysis is providing the discipline of gravimetric analysis. This is the process of weighing an isolated element or a definite compound of the element in as pure a form as possible, and has been defined as "quantitative analysis by weight".

The technique of thermogravimetry (TG) or thermogravimetric analysis (TGA), is monitoring the changes in mass of a sample against time or temperature while the temperature of the sample, in a specified atmosphere, is programmed. It offers high accuracy and stability [20, 29].

The apparatus is called a thermobalance or a thermogravimetric analyser, and consists of four major parts:

- the electrobalance and its controller
- the furnace and temperature sensors
- the programmer and computer
- the recorder, plotter or data acquisition device.

The thermobalance system is pictured in Figure 20 [20].

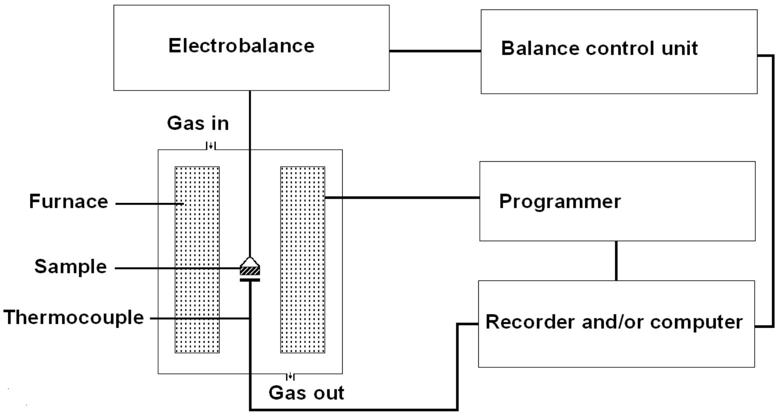

Figure 20: Schematic diagram of the thermobalance system [20].

7.1 The TGA

The balance used in many of the commercial apparatus is a modified electronic microbalance. There can be several different arrangements for the thermobalance, and the horizontal thermobalance is pictured in Figure 21. The lightweight arm is pivoted about an electrical coil suspended in a magnetic field.

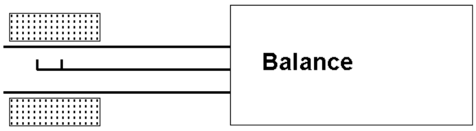

Figure 21: The horizontal thermobalance, showing the furnace (shaded region), sample position and casing [20].

It is important to maintain a constant position of the sample in the same zone of the furnace. Hence an optical sensor is measuring the position of the arm and any deflection is causing a current to be supplied to the coil which restores it to the “null” position. The sample which is suspended into the furnace from one arm of the balance is being counterbalanced by a tare. This tare can either be electrically applied to the coil or added to the reference pan. The resolution of the balance is often of 1 μg or better, and sample sizes can range from a few milligrams up to 30 g. As the balance is very sensitive, it is essential that it is free from vibration.

The furnaces are usually non-inductively wound electrical resistance heaters, and their temperature is measured by a thermocouple. The signal from the thermocouple is transmitted to the programmer and compared to that required by the programme set by the operator. If the temperature is too low, the system responds by supplying more power to the furnace, and if it is too high, it responds by reducing the power. For the balance to operate with as little interference as possible, another thermocouple is often measuring the sample temperature. This thermocouple is placed near to, but not in contact with the sample.

Thermogravimetry may be conducted in a flowing gas stream to control the evolution of gases from the sample. The sample can then be surrounded in an inert or reactive atmosphere. The flow of gas through the system can also help transferring heat and assist the transfer of products to an external gas analysis system. If the flow rate is too high it can disturb the balance mechanism, but if the flow rate is too low, it will not remove the gases or supply reactant gas. A flow rate of about 10-30 cm^3/min is often used [20].

8 Experimental

8.1 Experimental Setup

The Optical Microscope:
For the experiments a Stereomicroscope Stemi 2000-C from ZEISS, with a 7.7:1 zoom range was utilised. In contrast with other Stemi models, Stemi 2000-C possesses a tube which makes it possible to connect the microscope to a digital photo- or video camera [11, 12]. Stemi 2000-C, and the optical pathway of the electromagnetic ray, is pictured in Figure 22.

The Camera:
The camera attached to the optical microscope was a PixeLINK 1.3 Megapixel FireWire Cameras, model PL-A642. The camera receives power and communicates with the computer through a single FireWire cable. The software package, PixeLINK Capture, contains graphical controls to adjust the camera's imaging parameters, such as exposure, white balance and region of interest. It may capture colour or monochrome snapshot images and videos [40].

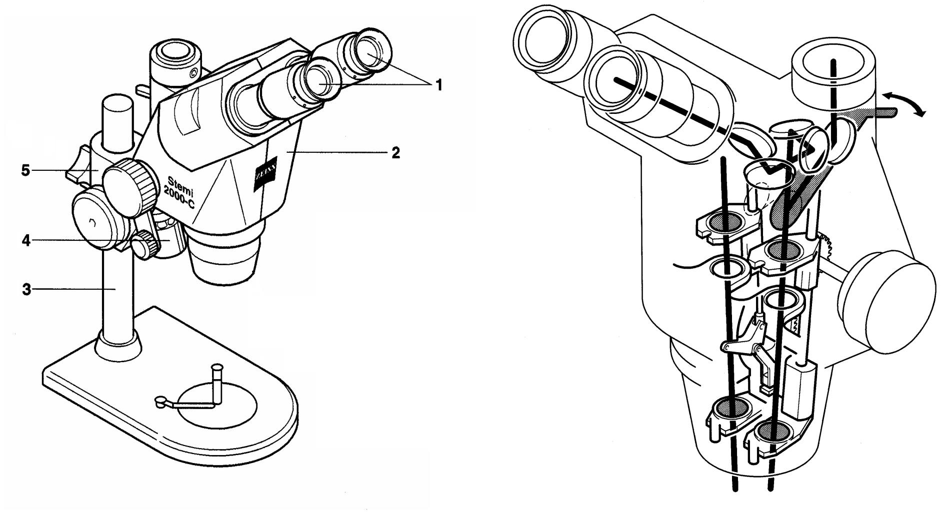

(a) (b)

Figure 22: In Figure (a), 1 corresponds to the eyepiece, 2 is the microscope body, 3 is the stand with a 260 mm column, 4 is the light guide holder and 5 is the Stemi mount with drive for column 32. In Figure (b) the optical pathway of the microscope is illustrated [12].

The AFM:
The AFM images were taken using a MultiMode$^{\text{TM}}$ Atomic Force Microscope from Veeco Instruments, operating in normal room air (see Figure 16(a)). The AFM can scan from the maximum scan size of 125 micron to a few nanometers with full 16-bit resolution on all scan waveforms and each axis. The MultiMode AFM has three different scanners for different scan sizes, which are pictured in

Figure 23 [51]. The A-scanner has a scan size of (0.4 × 0.4) μm, the E-scanner a size of (10 × 10) μm and the J-scanner has a size of (125 × 125) μm.

A complete range of AFM techniques for surface characterisation of properties can be performed with this high resolution tool. These include topography, elasticity, friction, adhesion and electrical/magnetic fields. It can also heat and cool samples for biological applications, polymers or other materials, and is able to scan samples in liquids. The MultiMode is today the most widely used AFM in the world [51]. The probes that are used for scanning in contact mode are NP Series Probes, model NP-20 from Veeco [53]. See Appendix D for details. The number of data points present in the image are restricted to 512, 256 and 128 for the MultiMode AFM [52].

Figure 23: The three scanners for the MultiMode AFM, J, E and A.

The TGA:
The TGA used for measuring the mass of the evaporating droplets is a TGA/SDTA851^e from Mettler Toledo, which provides a temperature accuracy of ± 0.25%. The measuring cell is gas-tight for definable measurement environment, and the sample range goes up to 900 μl. It takes about 5 minutes to heat the oven from room temperature up to 1100°C, which is the temperature range of the TGA. To cool the oven from 1000 to 100°C, however, takes 20 minutes. The furnace temperature and the time of the experiment is adjusted by using the software STAR^e [28].

8.2 Deposition Surfaces

For the experiments, two different substrates were used, normal or hydrophilic glass (wetting) and silanised or hydrophobic glass (non-wetting). To prepare the hydrophobic substrate, the glass had to be treated with a silanisation solution (Assay ~5% dimethyldichlorosilane in heptane, $C_2H_6Cl_2Si$). This was done to avoid the strong attraction of water that is present in normal hydrophilic glass, which makes the water spread out on the glass surface. The glass was treated by being lowered into the silanisation solution, and left there for a few minutes. The hydrophilic and hydrophobic surfaces are sketched in Figure 24.

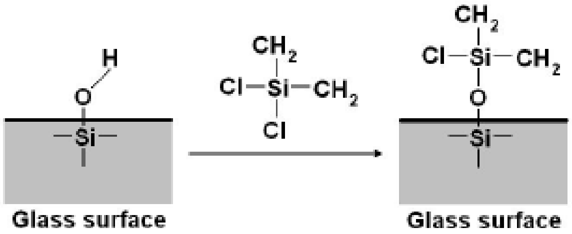

Figure 24: Silanisation of a glass surface with reactive chlorosilane [1].

8.3 Sample Preparation

Samples with 0.1, 0.2, 0.5 and 1.0 g of Laponite RD (see Appendix C) were prepared in 100 ml of demineralised water, to get concentrations of 0.1, 0.2, 0.5 and 1.0% respectively. The solutions were then stirred on the magnetic stirrer for a few hours, before they were filtered through filter paper of pore size 0.2 μm. The 1.0% sample, however, was too concentrated to filter, and therefore left unfiltered.

8.4 The Experiments

The experiments were conducted in ambient conditions, with an air temperature of about 21°C and a humidity of about 22%. Droplets of size 1 μl of the laponite suspensions or just pure water were placed on hydrophilic- and hydrophobic glass. The different samples were studied with the optical microscope and with the AFM in contact mode.

8.4.1 Study of Droplet Evolution

1 μl droplets, containing 0.5% laponite, were placed on both hydrophobic and hydrophilic glass surfaces and studied with the optical microscope. Pictures were taken from the top and the side, to see how the droplets evolved. Later the droplet depositions were scanned with the AFM in contact mode.

8.4.2 Radius versus Time

In this experiment the evolution of the radius of five different droplets was followed as a function of time for the different liquids and substrates. The droplets, with a volume of about 1 μl, were of either pure water or contained 0.5% laponite RD, and were deposited on hydrophilic and hydrophobic glass. The droplets were studied with the optical microscope as the water evaporated. Pictures were initially taken every minute, and more rapidly towards the end. Afterwards the radius was measured using the software Scanning Probe Image Processor (SPIP). Here the diameter of each droplet was measured 4 places, and the mean value was calculated.

8.4.3 Mass versus Time

Simultaneously with the measurements of the radius, we independently determined the mass of evaporating droplets with the TGA. Also the mass was measured for both hydrophilic and hydrophobic glass, with droplets of both pure water and 0.5% laponite, with three droplets of each sample. The initial volume was again about 1 μl. There was no air flow used, and the temperature was around 21°C. We measured the mass until it reached 0. The mean value of each sample was calculated and used for the evaluation of the results.

8.4.4 Study of Droplet Evolution with Crossed Polarisers

To find out if there were some ordering or just randomly distributed clay particles in the final deposit, the droplets were investigated through crossed polarisers attached to the optical microscope. Between the crossed polarisers, the birefringent samples appeared bright against the darker background.
The edge was later scanned with the AFM in contact mode, to see if we would get any consistency between the results.

9 Results

9.1 Crusting

It is evident that there is a formation of a skin or crust at the free surface of the laponite suspension drops, as seen in the figures below.

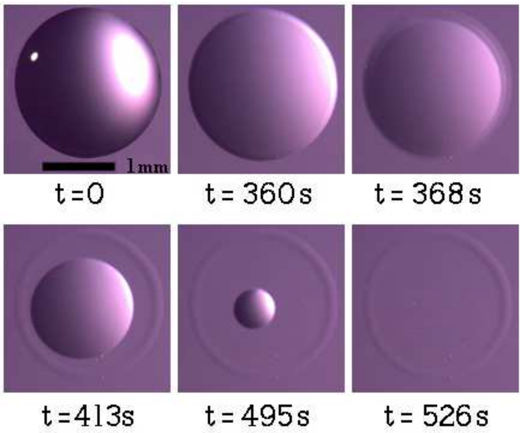

Figure 25: The evolution of a 0.5% laponite suspension droplet deposited on hydrophilic glass.

Figure 25 shows the evolution of a laponite suspension droplet on hydrophilic glass seen from above. The contact line is permanently pinned throughout the evaporation, and the cap is letting go of the foot after about 360 seconds. The end product is a circular clay deposit.

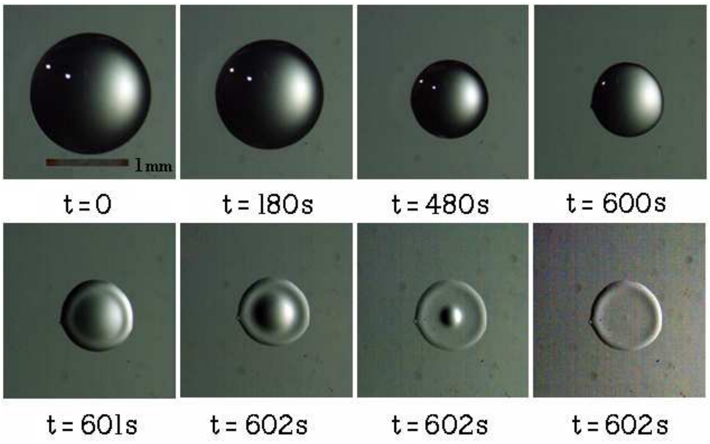

Figure 26: The evolution of a 0.5% laponite suspension droplet deposited on hydrophobic glass.

In Figure 26, one can see the evolution of a laponite suspension droplet on hydrophobic glass. The contact line is here pinned at about t = 600 seconds, which is where the foot and cap are starting to form. After that the evaporation is fast, and the droplet vanishes at about t = 602 s where it leaves a circular clay deposit.

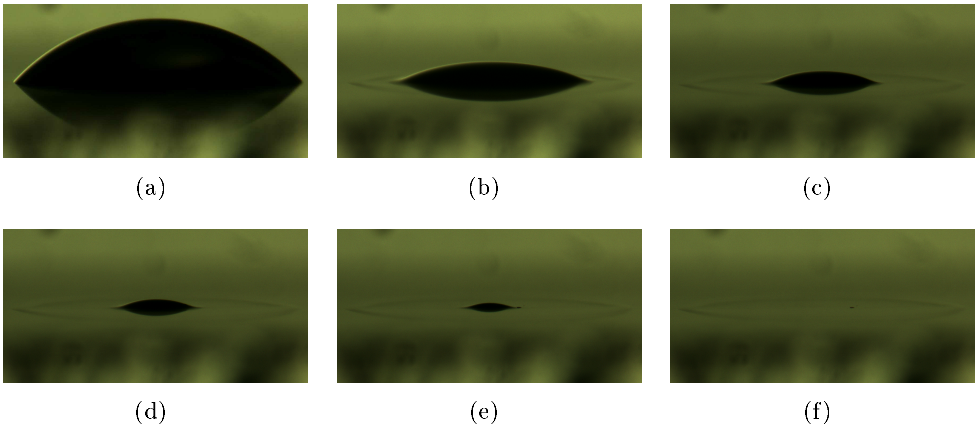

Figure 27: The formation of cap and foot in a droplet on a hydrophilic surface, viewed from the side.

Figure 27 shows the side view of the evolution of a laponite suspension drop on hydrophilic glass. As can be seen in the pictures the height is decreasing faster than the radius of the droplet and it is getting flatter as time goes by. The drop is "struggling" to keep the contact line pinned, but the cap and foot are separated in Figure 27(b), as could be seen in the droplets viewed from the top. The droplet is retaining an ellipsoidal cap shape throughout the whole evaporation process.

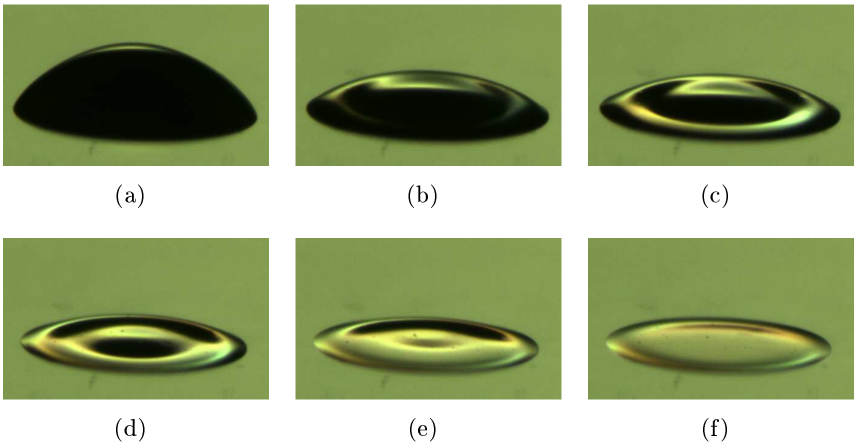

Figure 28: The formation of cap and foot in a droplet on a hydrophobic surface, viewed from the side.

As soon as the evaporation starts, particles from the suspension will deposit onto the substrate along the edge of the droplet. This is in turn leading to a strong anchoring of the contact line, which remains constant. In Figure 28 the end of the evaporation process (after the contact line has been pinned) of a suspension droplet on hydrophobic glass is pictured. We can observe distortions from an ellipsoidal cap shape, when a foot is forming near the edge. In contrast with the laponite suspension droplet on hydrophilic glass, the cap and foot are never totally separated. The cap keeps supplying the foot with the suspension, until it completely disappears as seen in Figure 28(f).

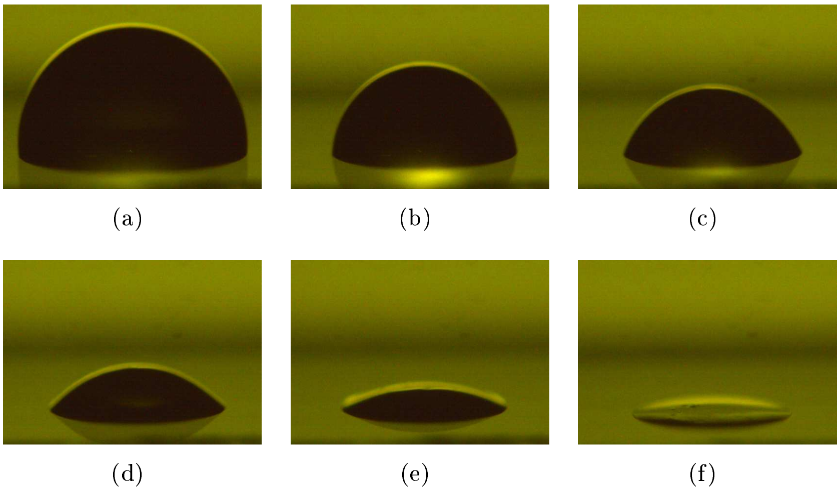

Figure 29: Evaporating suspension droplet on hydrophobic glass. Laponite concentration of 1%.

When a droplet of a higher concentration (1%) of laponite is evaporating, we do not get the same behaviour as for lower concentrated droplets (0.5%). For the first minutes of the evaporation it looks like a semi-sphere viewed from the side, as seen in Figure 29. In 29(c) it starts to flatten out, and ends up as a flat but thick stain 29(f). There is, however, no formation of cap and foot during the evaporation.

As can be seen in the figures of the droplets on both hydrophilic and hydrophobic glass, the height is decreasing much more rapidly than the radius. The contact angle is thus decreasing during the evaporation, in contrast with what Bonn et al. [42] got for their experiments with water droplets on mica. Instead they behave similar to what has earlier been shown for organic liquids.

When we studied the final deposit of a laponite suspension droplet on hydrophobic glass with the optical microscope, we found that the outer diameter of the droplet had decreased with almost 40%. The diameter of the hydrophilic droplet on the other hand had hardly decreased at all. This can be seen in Figures 30 and 31.

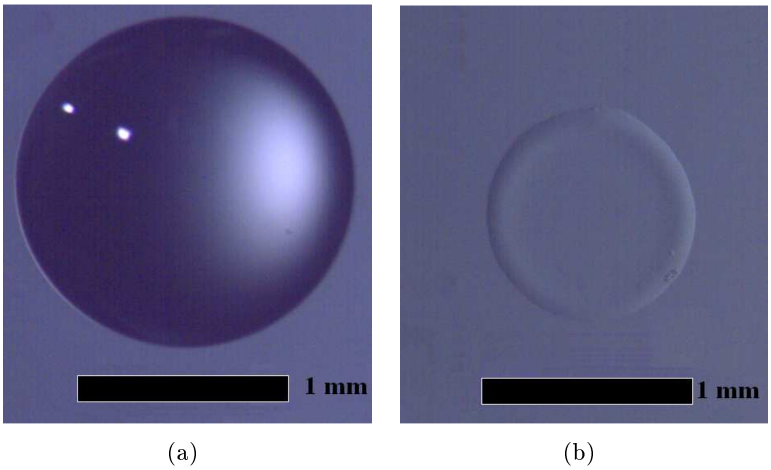

(a) (b)

Figure 30: (a) The initial and (b) the final stain of an evaporated laponite suspension droplet deposited on hydrophobic glass. The diameter of the initial droplet is about 1.6 mm and the diameter of the final stain is about 1.0 mm. The bar corresponds to 1 mm.

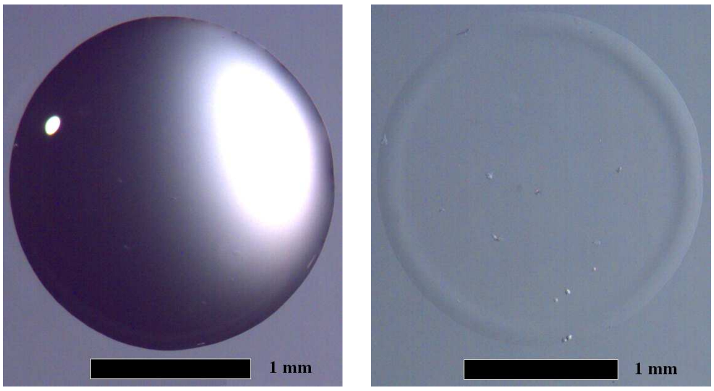

(a) (b)

Figure 31: (a) The initial and (b) the final stain of an evaporated laponite suspension droplet deposited on hydrophilic glass. The diameters of the initial droplet and the final stain are both about 2.0 mm. The bar corresponds to 1 mm.

The final stains were scanned with the AFM in contact mode to measure the thickness and height of the edges. The edge of the deposit on hydrophobic glass was found to be about 75 μm wide and about 4 μm high for a droplet with initial concentration of 0.5% laponite. The stain on the hydrophilic glass, however, has a height of only 350 nm, and a width of about 72 μm. The cross-section analysis can be seen in Figures 32 and 33.

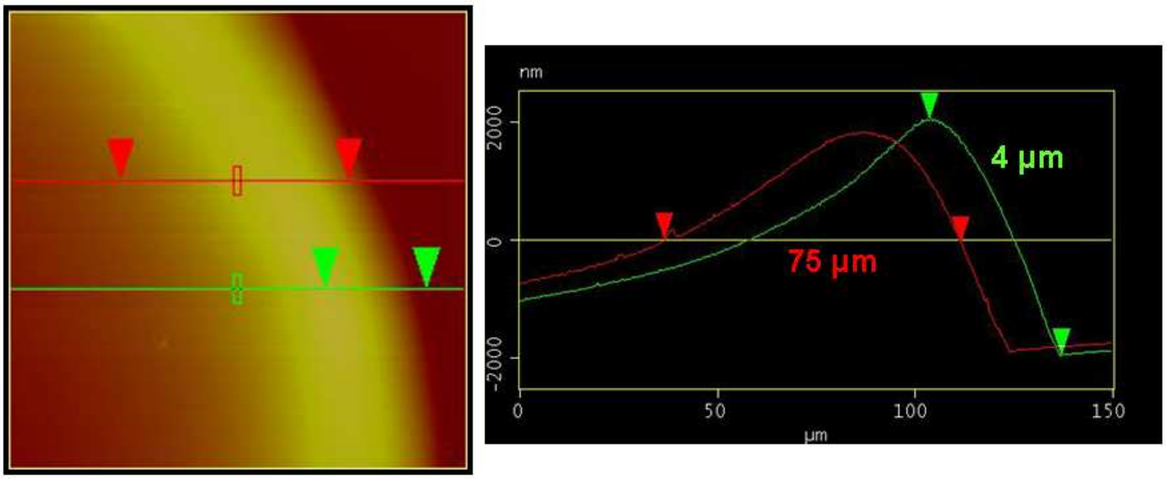

Figure 32: The profile of the clay deposit edge on hydrophobic glass.

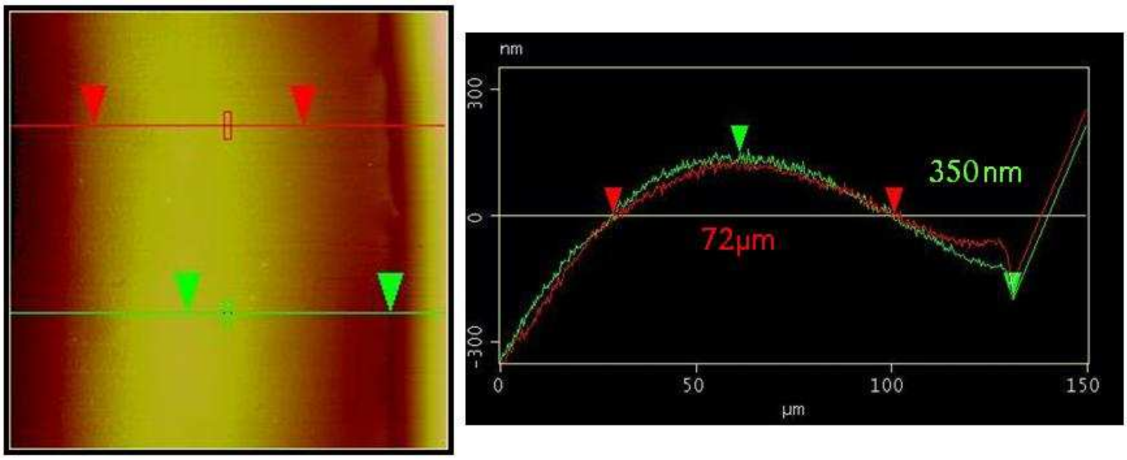

Figure 33: The profile of the clay deposit edge on hydrophilic glass.

Figures 34 show AFM scans of an evaporated 0.5% droplet on hydrophobic glass, scanned in the upper and lower right corners of the end deposit. Notice the difference in height between the edge and the immediate inside of the edge. The stain is at its highest on the ring, at the lowest on the inside of the ring, and then it gradually rises towards the centre. It will however not be as high in the middle as on the edge. The explanation for the edge stain is the coffee-stain effect, which is carrying the solute towards the edge of the evaporating droplet throughout the evaporation process. The Marangoni effect is responsible for the height increase towards the centre of the droplet.

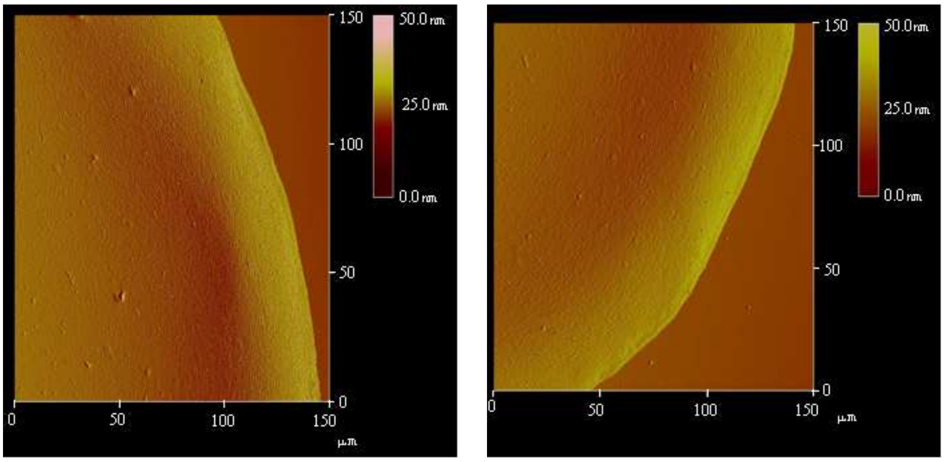

(a) (b)

Figure 34: The droplet scanned with the AFM at positions (a) upper, and (b) lower right corner.

If one inspects these two figures it seems like the larger agglomerates are arranged to point in different directions, which might be an indication of nematic ordering. This will be investigated further in Section 9.6.

As will later be seen in Sections 9.2, 9.4 and 9.5, the major reason that we are not getting the desired results is the irregular shape of the evaporating droplets. This can be seen in Figure 35, where the evolution of a 0.5% laponite suspension droplet on hydrophilic glass is pictured.

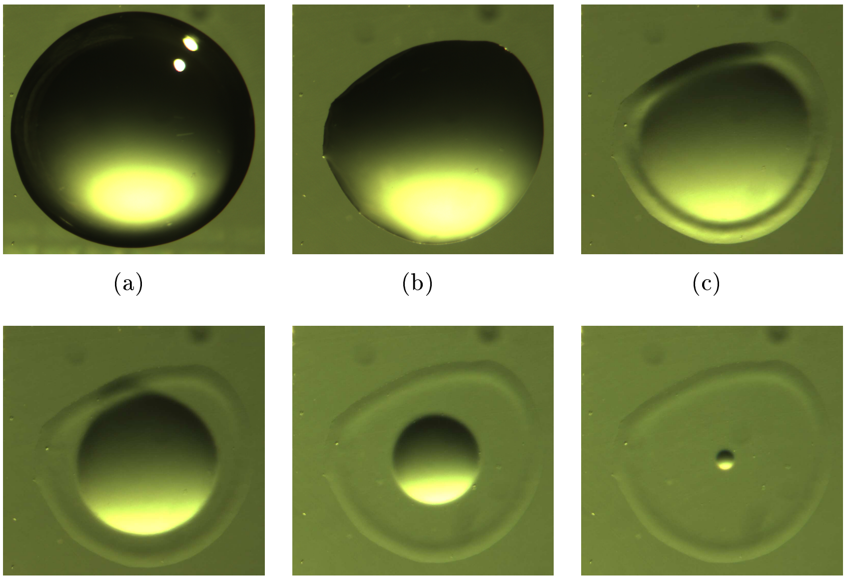

(a) (b) (c)

(d) (e) (f)

Figure 35: Non-circular suspension droplets on hydrophilic glass.

This irregular shape comes because of the pinning of the contact line, due to irregularities either on the substrate or in the suspension. To get the correct results it is therefore important to work with 100% clean equipment, and with a suspension where the suspended particles are evenly dispersed. The problem of non-circular droplets is most common for droplets on hydrophilic glass, where the pinning is not forced by silanisation.

9.2 Radius versus Time

The different values for the decreasing radius of droplets, containing water or a 0.5% laponite suspension, were evaluated versus time, and can be seen in Figure 36. It is important to realise that the radius followed is the radius of the inner part or cap of the droplet after the pinning of the contact line.

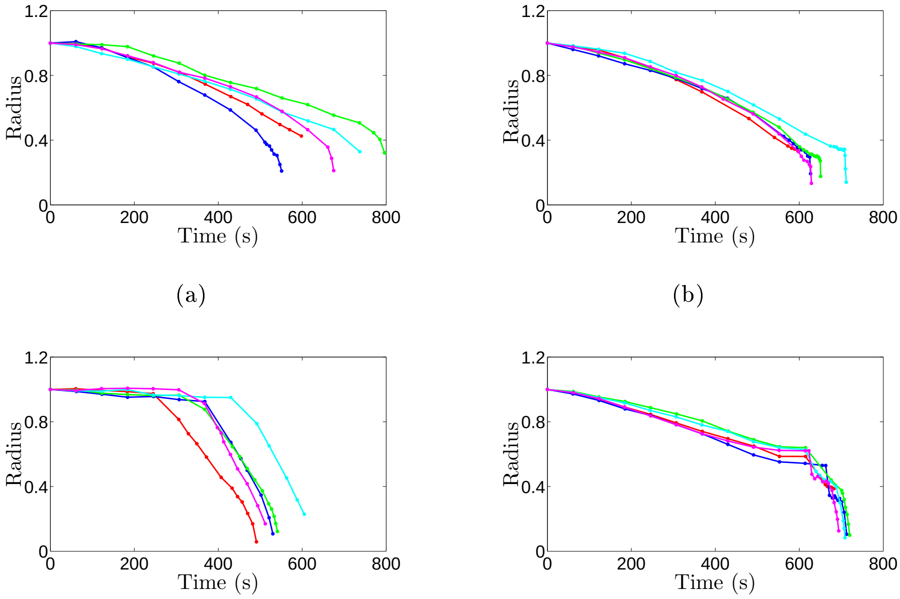

(a) (b)

(c) (d)

Figure 36: The normalised radius versus time, for (a) water droplets on hydrophilic glass, (b) Water droplets on hydrophobic glass, (c) laponite suspension droplets on hydrophilic glass and (d) laponite suspension droplets on hydrophobic glass.

The radius of the water droplets on hydrophilic glass have a more or less constant decreasing rate, and we get smooth curves as seen in Figure 36(a). For the laponite suspension droplets on hydrophilic glass, it is obvious from Figure 36(c) that the graph of the radius has two different evaporation regimes. Due to the contact line pinning of the droplet, the radius is at first constant, or evaporating very slowly. After about 200 - 400 seconds, the pinned edge is separated from the inner part of the droplet, where the evaporation is now much faster. The reason for this increase in evaporation is that the contact line of the inner part is not pinned, and thus the radius decreases faster. It might also be that most of the particles has been deposited onto the substrate, and the inner part of the droplet now contains a lower concentration of clay. As can be seen in Figures 36(b) and 36(d), the radius of the water droplets and the laponite suspension droplets deposited on hydrophobic glass both start with an almost constant decrease. After about 600 seconds, however, the behaviour of the suspension droplet suddenly changes. This is where the cap and foot are separated, and the droplet radius seems to have come to a halt, before it is decreasing much more rapidly. After entering the second evaporation regime, the droplets are disappearing in a couple of seconds. This agrees with what was earlier seen in Figures 25 and 26.

The results from the measurement of the radius were also evaluated by comparison of 1-R^2 versus time, where R is the normalised radius, and are pictured in Figure 37.

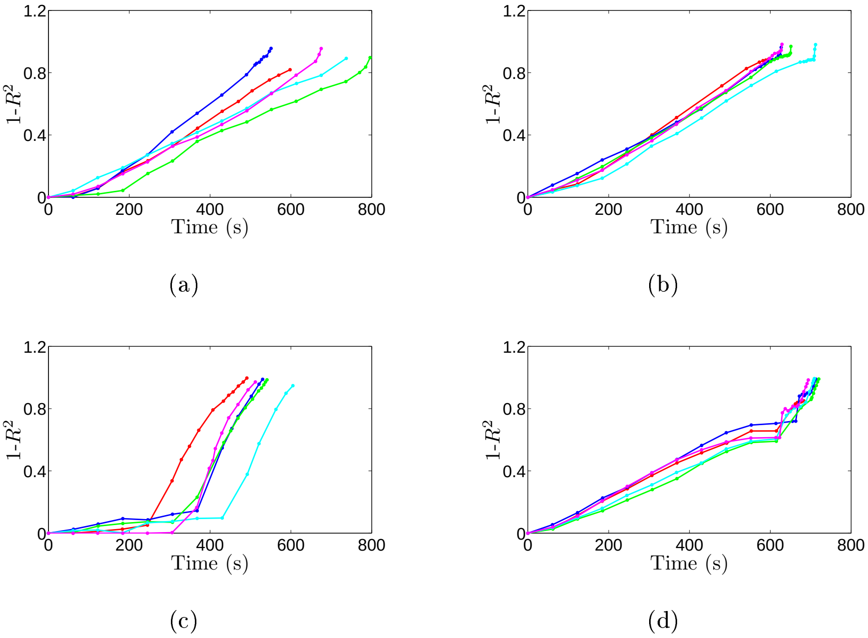

(a) (b)

(c) (d)

Figure 37: 1-R^2 versus time, where R is the normalised radius, and the time is measured in seconds. (a) water droplets on hydrophilic glass, (b) Water droplets on hydrophobic glass, (c) laponite suspension droplets on hydrophilic glass and (d) laponite suspension droplets on hydrophobic glass.

It can be seen from the figure that 1-R^2 is basically linear for all the graphs, although the linearity is present in two regimes for the suspension droplets. As mentioned in the Introduction, this means that the evaporation of the solvent is diffusive, and we can conclude that there is some diffusion present in the evaporating droplets.

The sources of error are many. A major error source is, however, the number of samples, and the number of pictures taken for each sample. The tools utilised for the experiments are not very accurate, and thus there is possibly a large error connected to the number of experiments. The experimental conditions might not have been the same for all the experiments, and equipment like the pipette and the substrates may have behaved differently from sample to sample. Another error source was that the droplets on hydrophilic glass were seldom totally circular, and with the irregular shapes, the measured radius contains an error.

9.3 Mass versus Time

The results from the measurements on the TGA were used to calculate the evaporation rate of the droplets. The curves are not totally linear, and therefore the results have a certain error, but they are an indication of how fast the droplets are evaporating. The values of the evaporation rates are given in Table 1.

Sample	Evaporation rate
Hydrophilic - water	$\sim 1.26 \times 10^{-3}$ mgs^{-1}
Hydrophobic - water	$\sim 2.02 \times 10^{-3}$ mgs^{-1}
Hydrophilic - 0.5% laponite	$\sim 2.47 \times 10^{-3}$ mgs^{-1}
Hydrophobic - 0.5% laponite	$\sim 1.98 \times 10^{-3}$ mgs^{-1}

Table 1: The evaporation rates of the four different samples.

For the hydrophobic surfaces, the evaporation rate is almost the same, about 2×10^{-3} mgs^{-1}, for the droplets of pure water and the droplets of the 0.5% laponite suspension. The laponite suspension droplet on hydrophilic glass, on the other hand, has a 96% faster evaporation rate than the water droplet on the same surface. Our results are somewhat lower than those of Bonn et al. [42], who found the evaporation rate to be about 3×10^{-3} mgs^{-1} for distilled water on a mica surface. The reason for this difference might be due to the fact that mica is very hydrophilic. The initial droplet spreads out over a large area, and thus gets a larger surface area, which leads to faster evaporation. The glass is more hydrophobic, and also has a few irregularities in the surface structure, where the droplet may get pinned. Then the surface area of the droplet is smaller, and the evaporation slower. The graph of the mass versus time is presented in Figure 38.

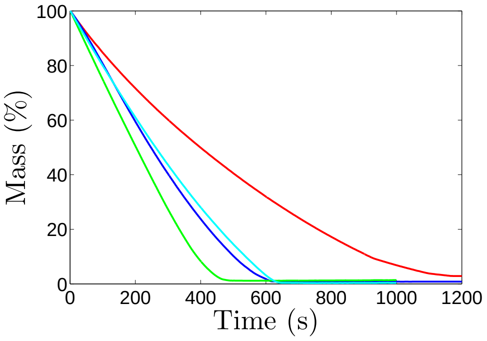

Figure 38: The mass of the droplets (in %) plotted versus time (in seconds). The red, blue, green and light blue curves correspond to water droplets on hydrophilic glass, water droplets on hydrophobic glass, laponite suspension droplets on hydrophilic glass and laponite suspension droplets on hydrophobic glass respectively.

9.4 How the Radius Scales with Time

As earlier mentioned, $R \propto \sqrt{t_0 - t}$, where t_0 is the time where the droplet vanishes, is expected where the evaporation is purely diffusive. We concluded that there was diffusion present in the droplets in Section 9.2, and also wanted to test this prediction mathematically.

The data of the decreasing radius for 5 different droplets were fitted to the power-law behaviour, $R = C_R(t_0 - t)^{\alpha_R}$, where the values of C_R and α_R were found using the method of least squares which is described in Appendix A. These values are displayed in Tables 2 through 5, together with the mean values, $\bar{x}$, and the standard deviations, σ (see Appendix B). The theoretical values are also plotted against the 5 experimental ones in Figures 39 through 42.

9.4.1 Water Droplets on Hydrophilic Glass

	C_R	α_R
1	0.17360	0.29460
2	0.13960	0.34860
3	0.17000	0.26700
4	0.08900	0.35660
5	0.16290	0.29140
$\bar{x}$	0.14702	0.31164
σ	0.03133	0.03487

Table 2: The constant C_R and the exponent α_R for 5 different water droplets on hydrophilic glass.

We can see from Table 2 that the value for α_R is about 0.3, while the constant C_R is between 0.1 and 0.2. The standard deviation is about 0.03 for both of them.

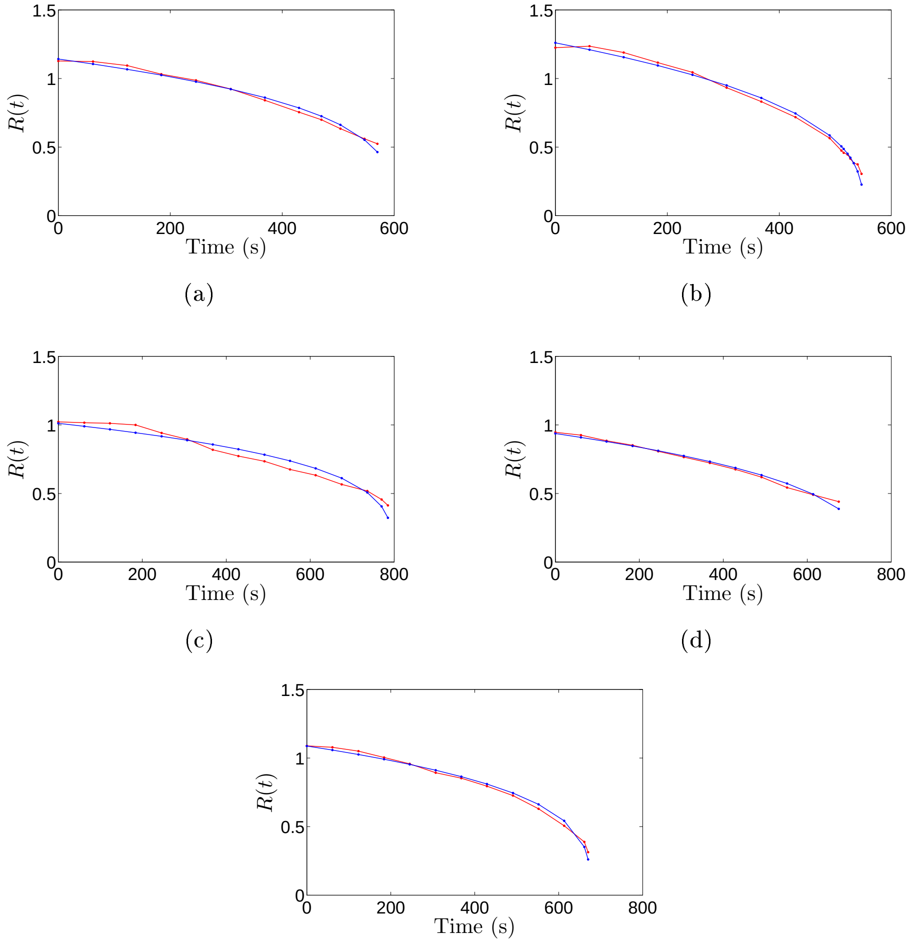

(a) (b)

(c) (d)

(e)

Figure 39: The radius, $R(t)$ (measured in mm), for the 5 water droplets on hydrophilic glass plotted against time. The red curve represents the experimental-, and blue represents the theoretical value.

The theoretical values with the constant and exponent from above, is a good match with the experimental values, as can be seen in Figure 39. The relation between R and $t_0 - t$ of water droplets on hydrophilic glass is thus $R = C_R(t_0 - t)^{\alpha_R}$, with $C_R = 0.14702 \pm 0.03133$, and $\alpha_R = 0.31164 \pm 0.03487$.

9.4.2 Water Droplets on Hydrophobic Glass

	C_R	α_R
1	0.10970	0.28960
2	0.10230	0.29790
3	0.09360	0.30860
4	0.11890	0.27660
5	0.07810	0.34380
$\bar{x}$	0.10052	0.30330
σ	0.01397	0.02279

Table 3: The constant C_R and the exponent α_R for 5 different water droplets on hydrophobic glass.

We can see from Table 3 that the value for α_R is about 0.3, while the constant C_R is about 0.1. The standard deviation is about 0.01 and 0.02 for the constant and exponent respectively.

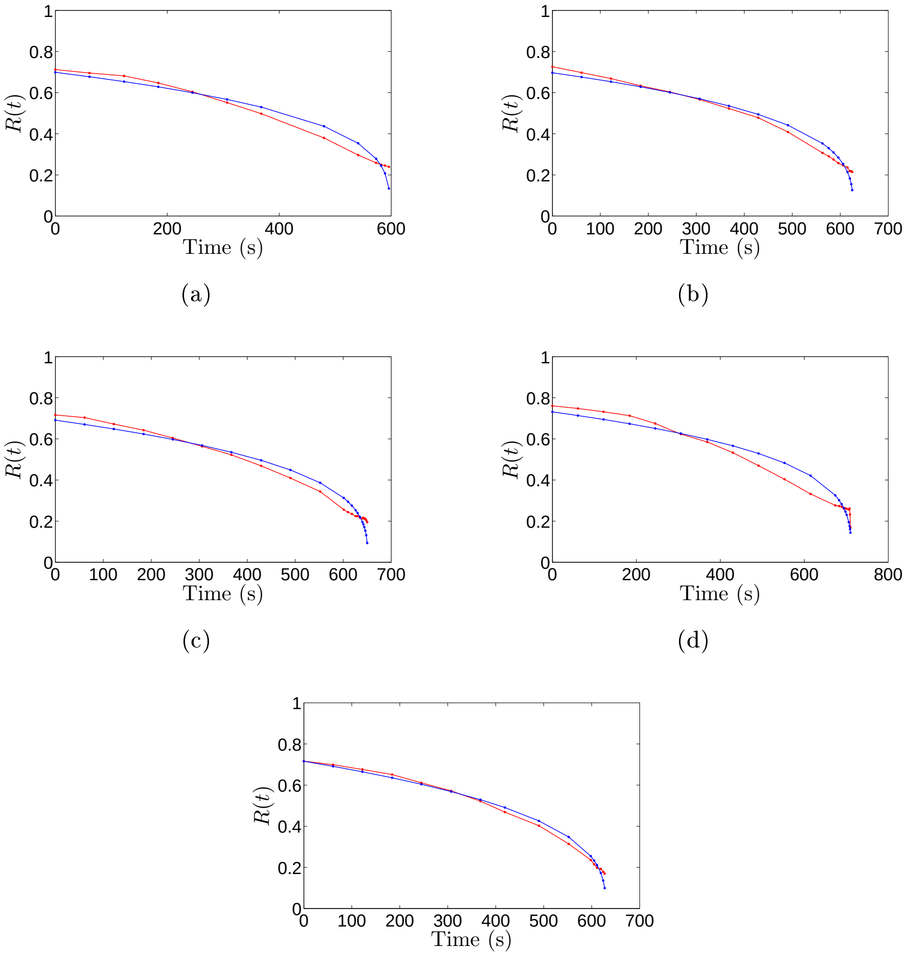

(a)

(b)

(c)

(d)

(e)

Figure 40: The radius, R(t) (measured in mm), for the 5 water droplets on hydrophobic glass plotted against time. The red curve represents the experimental-, and blue represents the theoretical value.

The theoretical values with the constant and exponent from Table 3, is a good match with the experimental values for the water droplet on hydrophobic glass as well, as can be seen in Figure 40. The evaporation can here be characterised by $R = C_R(t_0 - t)^{\alpha_R}$, with $C_R = 0.10052 \pm 0.01397$, and $\alpha_R = 0.30330 \pm 0.02279$.

9.4.3 Laponite Suspension Droplets on Hydrophilic Glass

	C_R	α_R
1	0.08740	0.44930
2	0.15940	0.31900
3	0.13080	0.35930
4	0.22620	0.25460
5	0.16910	0.31200
$\bar{x}$	0.13486	0,33500
σ	0.04569	0.06454

Table 4: The constant C_R and the exponent α_R for 5 different droplets of a 0.5% laponite suspension on hydrophilic glass.

We can see from Table 4 that the value for α_R is between 0.25 and 0.45, with a mean value of 0.3, while the constant C_R is between 0.09 and 0.23, with a mean value of 0.1. The standard deviation is about 0.05 and 0.06 for the constant and exponent respectively.

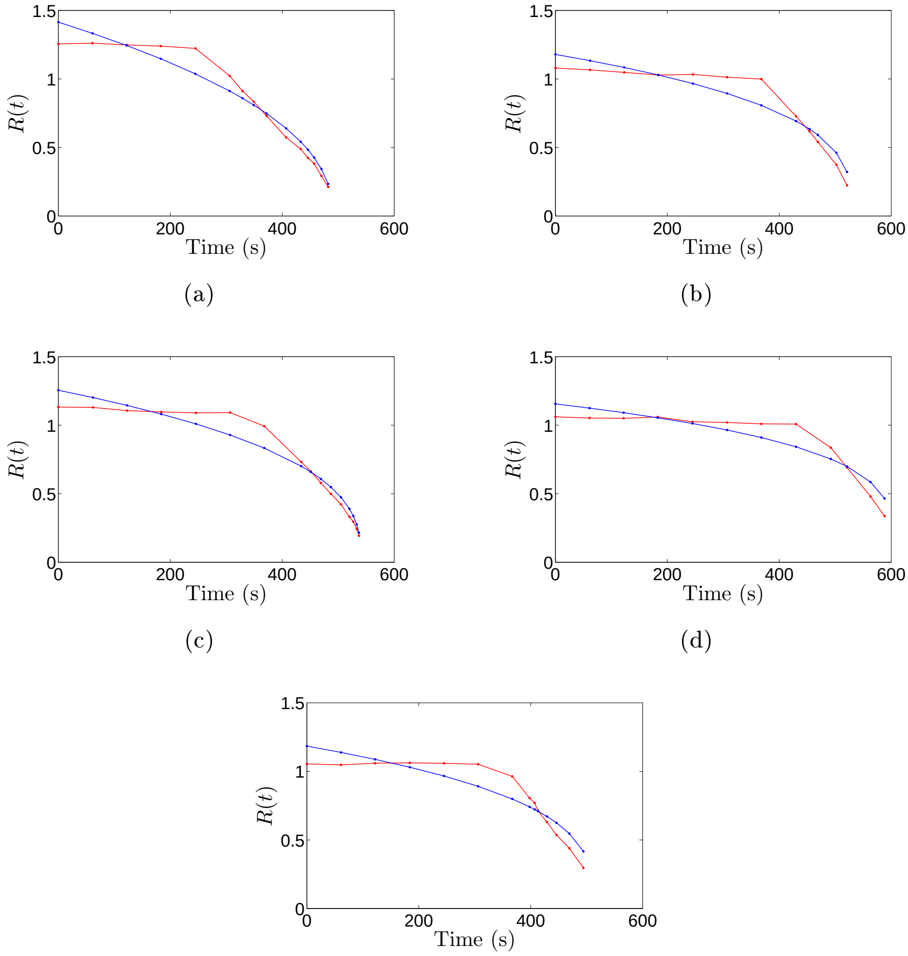

(a)

(b)

(c)

(d)

(e)

Figure 41: The radius, R(t) (measured in mm), for the 5 0.5% laponite suspension droplets on hydrophilic glass plotted against time. The red curve represents the experimental-, and blue represents the theoretical value.

The theory does not match as well for the laponite suspension droplet deposited on hydrophilic glass, as can be seen in Figure 41. The model is not as suitable for the curve with two evaporation regimes. However, it is an indication of the behaviour, and we may characterise the evaporation by $R = C_R(t_0 - t)^{\alpha_R}$, with $C_R = 0.13486 \pm 0.04569$, and $\alpha_R = 0{,}33500 \pm 0.06454$.

9.4.4 Laponite Suspension Droplets on Hydrophobic Glass

	C_R	α_R
1	0.16380	0.23020
2	0.09860	0.30810
3	0.11690	0.29100
4	0.11370	0.29370
5	0.13050	0.27030
$\bar{x}$	0.12470	0.27866
σ	0.02202	0.02706

Table 5: The constant C_R and the exponent α_R for 5 different droplets of a 0.5% laponite suspension on hydrophobic glass.

We can see from Table 5 that the value for α_R is about 0.3, while the constant C_R is about 0.1. The standard deviation is about 0.02 and 0.03 for the constant and exponent respectively.

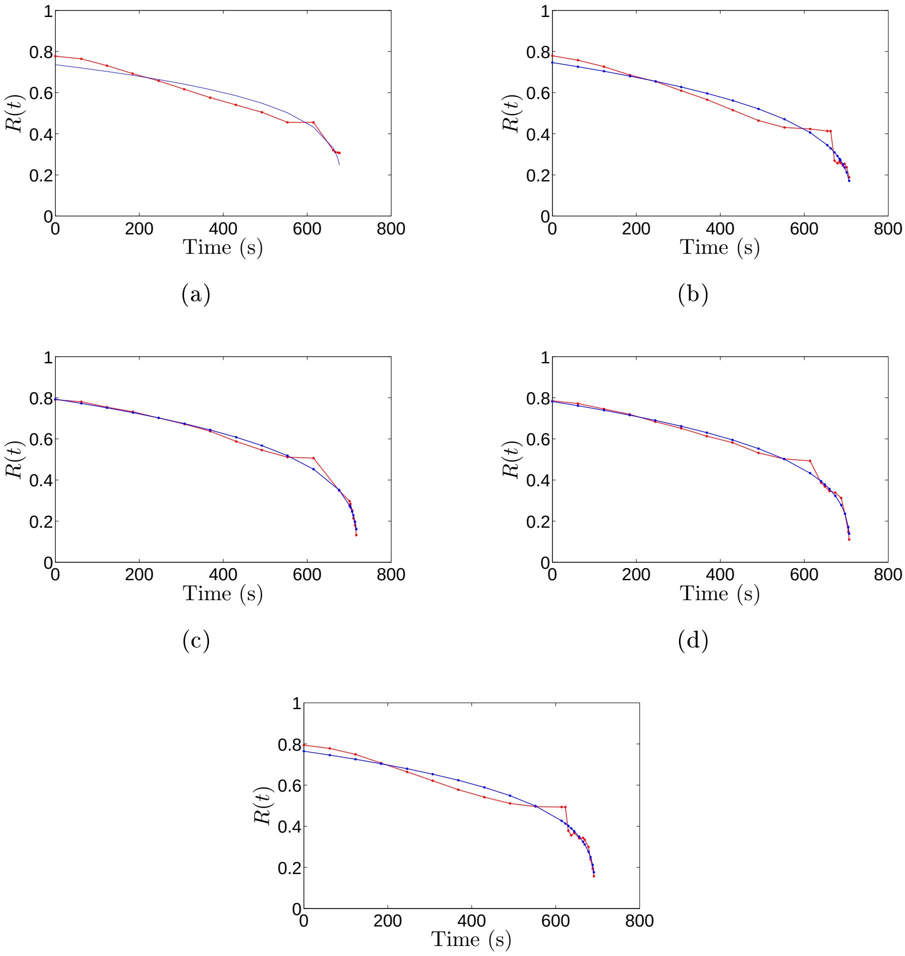

(a) (b) (c) (d) (e)

Figure 42: The radius, R(t) (measured in mm), for the 5 0.5% laponite suspension droplets on hydrophobic glass plotted against time. The red curve represents the experimental-, and blue represents the theoretical value.

The theoretical values with the constant and exponent from above, are again a good match with the experimental values for the laponite suspension droplet on hydrophobic glass, as we can see in Figure 42. This is apart from an irregularity after about 600 seconds, at the beginning of the second evaporation regime. This is about when the cap and foot is forming in these droplets, after which the evaporation is considerably faster. The evaporation can here be characterised by $R = C_R(t_0 - t)^{\alpha_R}$ with $C_R = 0.12470 \pm 0.02202$, and $\alpha_R = 0.27866 \pm 0.02706$.

The conclusion from a number of experiments is that the evaporation can be characterised by: $R(t) = C_R(t_0 - t)^{\alpha}_{R}$, where R is the radius of the drop, and α_R and C_R is presented in Tables 2 through 5. The mean value found for the exponent α_R is about 0.3, while the mean value for the constant C_R is about 0.13. Both the results are significantly different from what has previously been found, and also compared to the criterion for pure diffusivity, α_R=0.5. Hence we can not conclude from these results that the evaporation is diffusive. We can also see from the graphs that the radius and evaporation time is depending on the substrates and whether the droplet contains laponite or not. As would be expected, due to lack of pinning, the water droplet on hydrophilic glass has the largest initial radius. The smallest, however, is not obtained for the suspension droplet on hydrophobic glass, but rather for the water droplet deposited here. The highest evaporation rate is seen for the laponite suspension droplet on hydrophilic glass, with a mean evaporation time of about 550 seconds. The laponite suspension droplets on hydrophobic glass have the lowest evaporation rate, and has a mean evaporation time of more than 700 seconds.

Bonn et al. [42], found values for the constant and exponent to be $\alpha_R = 0.61\pm0.03$ and $C_R = 0.1\pm0.04$. These results, however, were of water droplets on mica, and the difference might be due to the hydrophilic nature of mica, and hence a much higher evaporation rate is observed.

There is also here a large error factor connected to the results. This error is much because of the number of droplets studied, and due to the fact that many of the droplets were non-circular. In addition there is also a large human error factor, when measuring the radius manually.

9.5 How the Volume Scales with the Radius

It was also interesting to investigate how the volume and the radius of the droplets were related. The experimental data were again fitted to a power-law behaviour, $V = C_V R^{\alpha_V}$, where the values of C_V and α_V were found using the method of least squares. These values are displayed in Tables 6 through 9 together with the standard deviation. The values for the volume are also plotted together with the values found by $C_V R^{\alpha_V}$ in Figures 43 through 46. The experimental values for the radius were found for 5 different droplets of each surface and suspension. The experimental values for the volume where found averaging the 3 droplets that had been measured with the TGA for each substrate and suspension. As $m = \rho V$ and $\rho = 1\frac{\text{mg}}{\text{mm}^3}$, $m = V$, and the values for the mass could thus be used directly as the volume.

9.5.1 Water Droplets on Hydrophilic Glass

	C_V	α_V
1	0.8171	1.4672
2	0.7908	0.7952
3	0.9090	2.1070
4	1.1492	1.8895
5	0.8442	1.5255
$\bar{x}$	0.9021	1.5569
σ	0.1297	0.4478

Table 6: The constant C_V and the exponent α_V for water droplets on hydrophilic glass.

The values found here are not as consistent as the values for R versus $t_0 - t$, and it can be seen from Table 6 that the mean value for α_V is 1.6, while the constant C_V has a mean value of 0.9. The standard deviation is about 0.13 and 0.45 for the constant and exponent respectively.

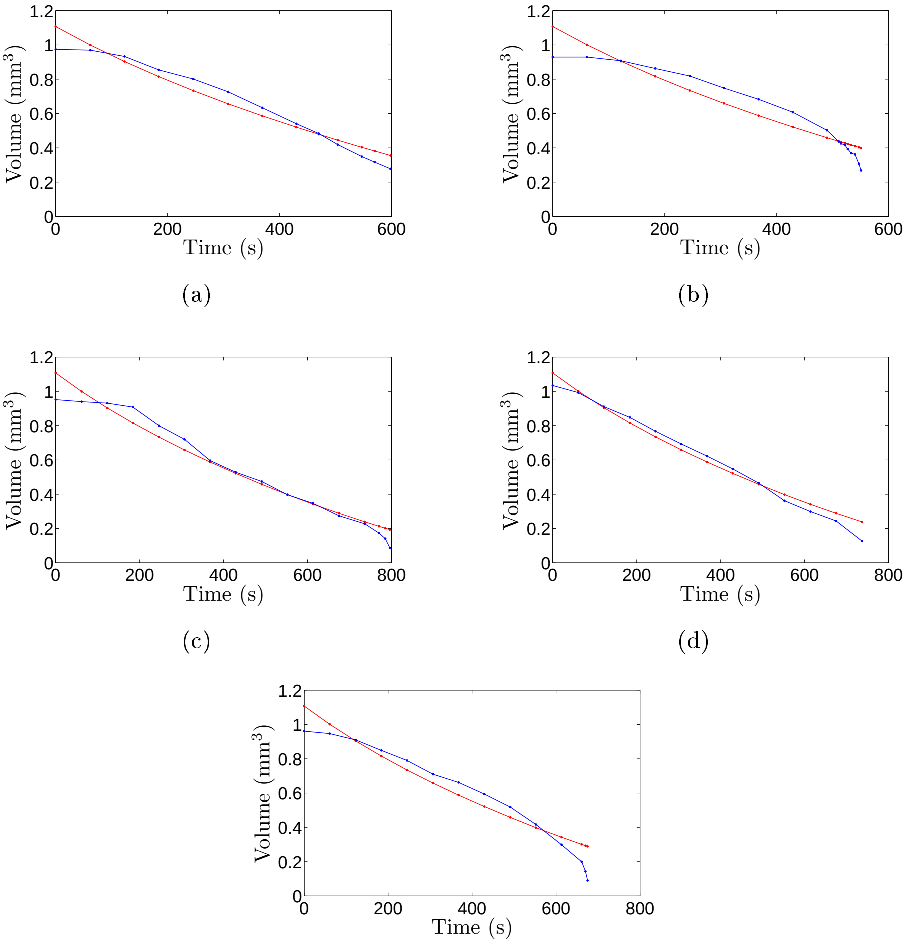

(a) (b) (c) (d) (e)

Figure 43: Water droplets on hydrophilic glass. The red curve represents V, and blue represents the $C_V R^{\alpha_V}$.

As can be seen in Figure 43, the theoretical values with the constant and exponent from above, are not resulting in a good match between the volume and radius for the water droplets on hydrophilic glass. If this model is going to be used on the values, the relationship between the volume and radius can be characterised by $V = C_V R^{\alpha_V}$ with $C_V = 0.9021 \pm 0.1297$, and $\alpha_V = 1.5569 \pm 0.4478$.

9.5.2 Laponite Suspension Droplets on Hydrophilic Glass

	C_V	α_V
1	0.1504	30.0036
2	0.3763	9.3054
3	0.2723	4.4313
4	0.2535	18.7070
5	0.0638	22.0112
$\bar{x}$	0.2233	16.8917
σ	0.1072	9.1021

Table 7: The constant C_V and the exponent α_V for 0.5% laponite suspension droplets on hydrophilic glass.

Similar to the values found for the water droplets on hydrophilic glass, the values in Table 7 are not very consistent either. The values for α_V are ranging from 4 to 30 with a mean value of 17. The values for C_V, however, are a little more alike, with a mean value of 0.22. The standard deviation for C_V is 0.1 while it for α_V is as large as 9.

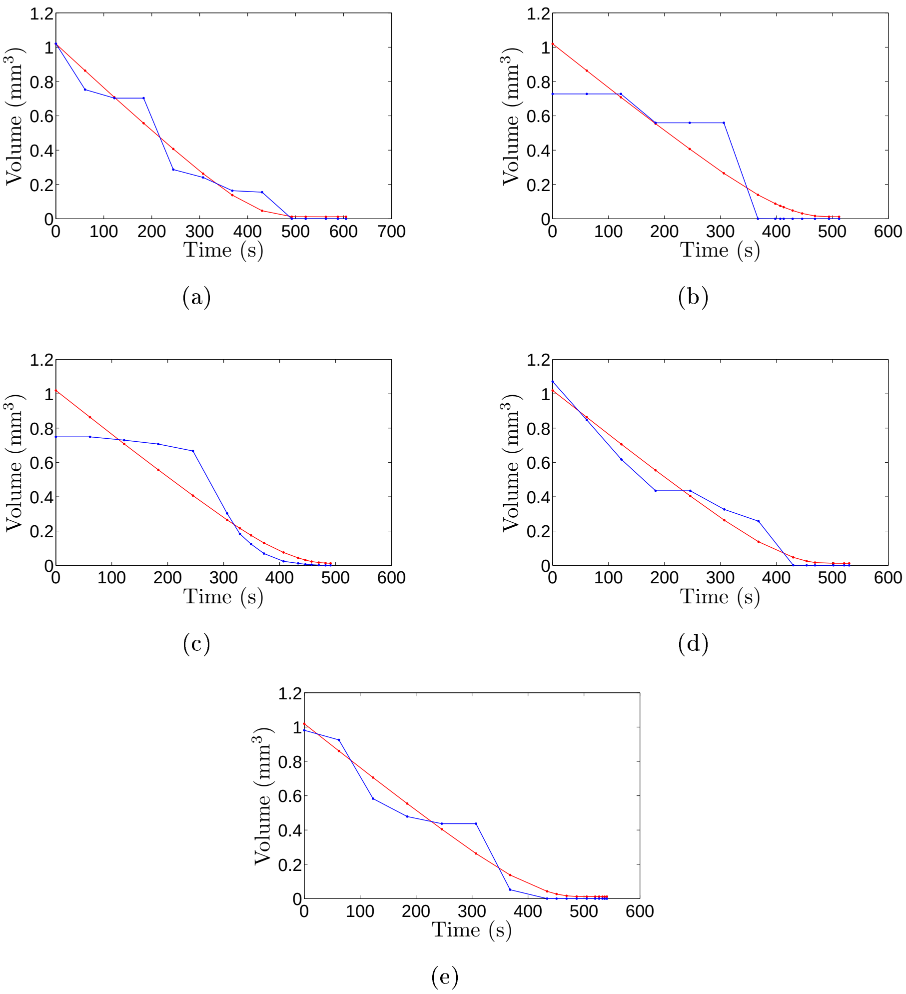

(a)

(b)

(c)

(d)

(e)

Figure 44: 0.5% laponite suspension droplets on hydrophilic glass. The red curve represents V, and blue represents the $C_V R^{\alpha_V}$.

As seen in Figure 44 there is not a good match between the radius and volume of the laponite suspension droplets on hydrophilic glass with the constants and exponents displayed in the table above. With the model $V = C_V R^{\alpha_V}$, $C_V = 0.2233 \pm 0.1072$ and $\alpha_V = 16.8917 \pm 9.1021$.

9.5.3 Water Droplets on Hydrophobic Glass

	C_V	α_V
1	3.5688	3.5658
2	3.8830	3.8010
3	3.9981	3.8756
4	3.9437	4.7852
5	4.0751	3.9506
$\bar{x}$	3.8937	3.9956
σ	0.1743	0.4153

Table 8: The constant C_V and the exponent α_V for water droplets on hydrophobic glass.

The values in Table 8 are more consistent than for the hydrophilic cases, with an α_V around 4, and a C_V around 3.9. The standard deviations are still high, with 0.17 and 0.42 for C_V and α_V respectively.

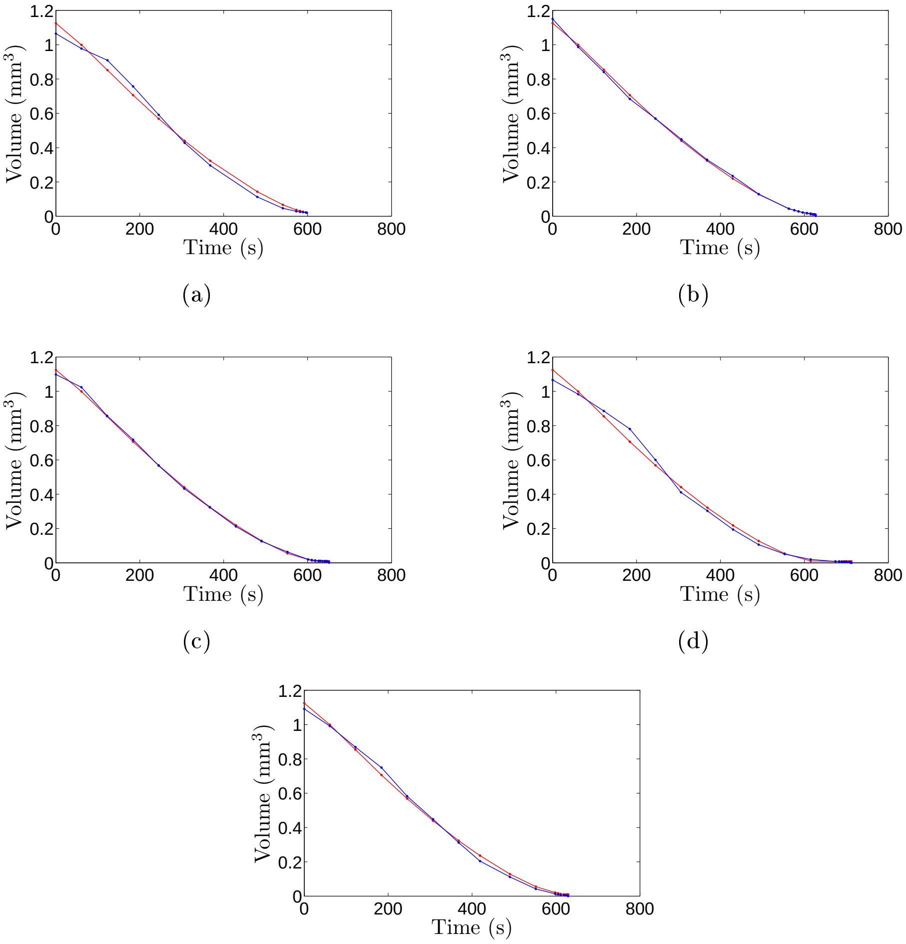

(a) (b) (c) (d) (e)

Figure 45: Water droplets on hydrophobic glass. The red curve represents V, and blue represents the $C_V R^{\alpha_V}$.

Even though the standard deviation for water droplets on hydrophobic glass was high, it can be seen in Figure 45 that the model $C_V R^{\alpha_V}$ is almost a perfect match with the volume, for the $C_V = 3.8937 \pm 0.1743$, and $\alpha_V = 3.9956 \pm 0.4153$. This is the best match we got for the model.

9.5.4 Laponite Suspension Droplets on Hydrophobic Glass

	C_V	α_V
1	3.1040	4.1615
2	2.9399	3.9115
3	3.6623	5.2474
4	3.5461	4.8934
5	2.9591	4.2901
$\bar{x}$	3.2423	4.5008
σ	0.3031	0.4936

Table 9: The constant C_V and the exponent α_V for 0.5% laponite suspension droplets on hydrophobic glass.

The values in Table 9 are not as consistent as for the water droplets on hydrophobic glass, with an α_V of about 4.5, and a C_V of about 3.2. The standard deviations are also a little higher with 0.30 and 0.49 for C_V and α_V respectively.

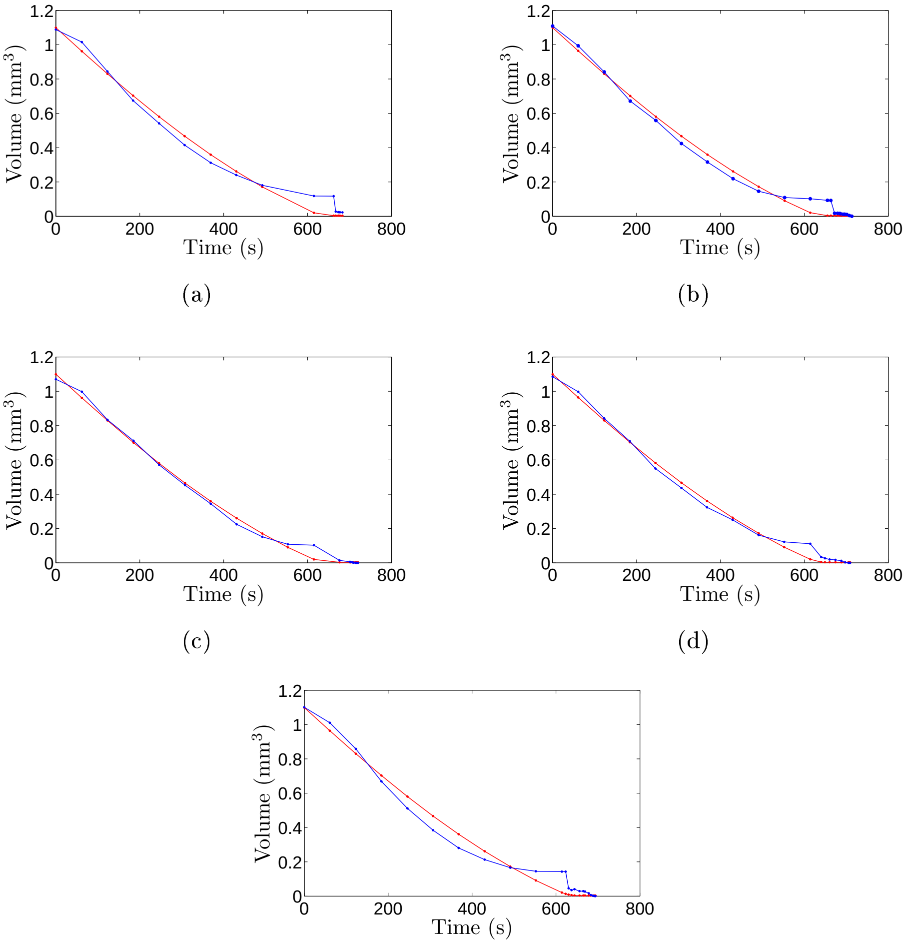

(a) (b) (c) (d) (e)

Figure 46: 0.5% laponite suspension droplets on hydrophobic glass. The red curve represents V, and blue represents the $C_V R^{\alpha_V}$.

For the laponite suspension droplets on hydrophobic glass, $C_V R^{\alpha_V}$ is a good model for the beginning of the evaporation process, as seen in Figure 46. After around 500 seconds there is a plateau for the measured values of R and hence a plateau for the values of $C_V R^{\alpha_V}$. This is where the laponite suspension droplets start dividing into cap and foot, and the radius seems to be constant for a while. $V = C_V R^{\alpha_V}$, with $C_V = 3.2423 \pm 0.3031$, and $\alpha_V = 4.5008 \pm 0.4936$, is a good model until about 500 seconds.

Bonn et al. [42] found that the volume of a hexane droplet deposited on mica was proportional to R^3, which is what would be expected if the droplet remained a spherical cap, with a constant contact angle during the evaporation. For water droplets on mica the volume is proportional to $R^{2.3}$. With water- and laponite suspension droplets deposited on glass, the conditions are quite different than for the hexane and water on mica, and consequently one can not expect to get the same values. Our closest match, compared to the results of water droplets on mica, is for water droplets on hydrophilic glass, with a mean α_V of ~1.6. This is also the situation which is most similar to water on mica, and therefore not very surprising. The water droplets on hydrophobic glass is resulting in the closest match with the hexane droplet on mica, with a mean α_V of ~4.0.

The reason for the difference between the two graphs in each figure is mainly because of the plateaus (for the suspension samples), and due to the large error in the measured radius. The model used for the evaluation does not take irregularities into account, and we experience large differences between the theoretical model and the observed values. The differences between the graphs are most evident in Figures 43 and 44, and is due to the non circular droplets which made it hard to get a reasonable value for the average radius of each droplet. For Figure 44 this is particularly bad, something which is also evident from Table 7. We can here see how the values for α_V are ranging between 4 and 30, giving a standard deviation of 9. With these results one can not conclude that this model is a good model for the relationship between the volume and radius.

9.6 Ordering

9.6.1 Birefringence

The laponite suspension droplets are showing optical birefringence in the foot, when viewed between a pair of crossed polarisers. This demonstrates that there exists a liquid-crystalline order of the plate-like particles, which is extending over macroscopic distances.

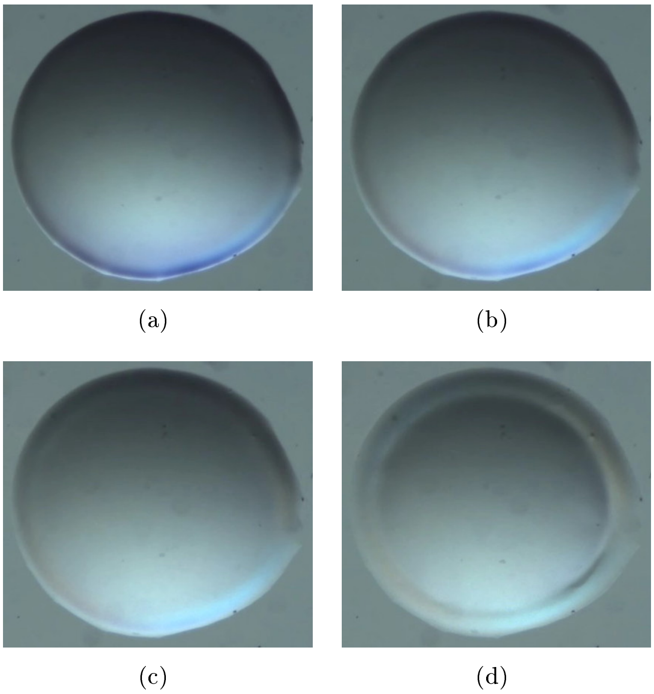

Figure 47: Birefringence in a laponite suspension droplet deposited on hydrophilic glass.

There is, to a certain extent, birefringence present for the laponite suspension droplet on hydrophilic glass (Figure 47), but it disappears when the cap and foot are separated. The droplet is red in the lower left and upper right corners, and blue in the lower right and upper left corner.

The birefringence is, however, more obvious for the hydrophobic glass than for the hydrophilic, as seen in Figure 48. The fact that there is more evident birefringence for the droplet on the hydrophobic glass surface might be due to a rougher surface. The particles can then easier settle down in a regular pattern, and give rise to the birefringence. This is typical of the nematic phase.

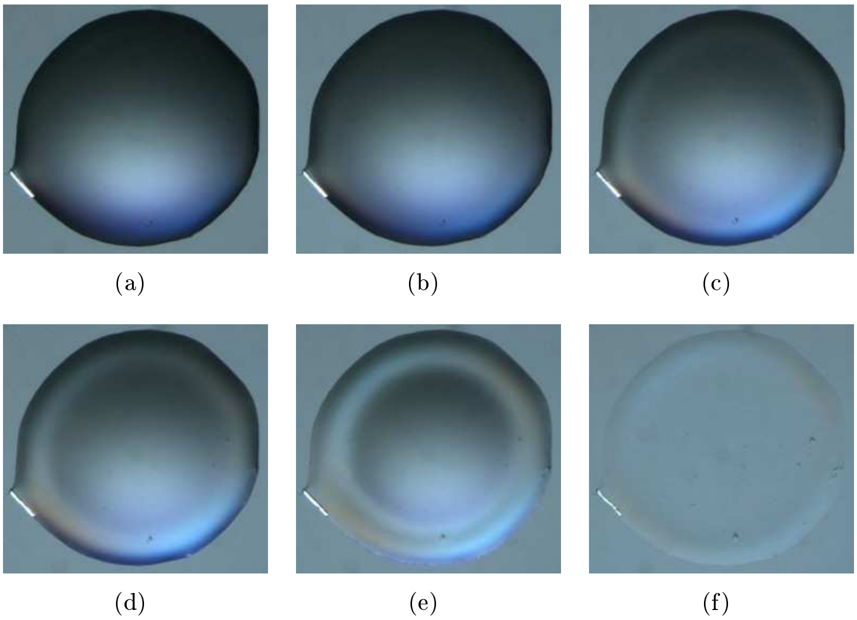

(a) (b) (c) (d) (e) (f)

Figure 48: Birefringence in a laponite suspension droplet deposited on hydrophobic glass.

9.6.2 Nematic Ordering

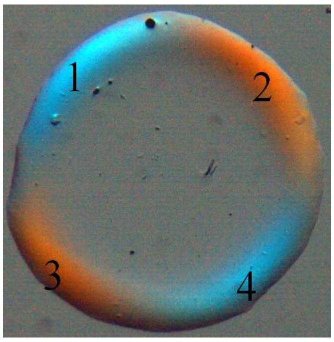

Figure 49: The final stain for the laponite suspension droplet on hydrophobic glass, with enhanced colours. The numbers correspond to the different positions of the ring that have been scanned with the AFM.

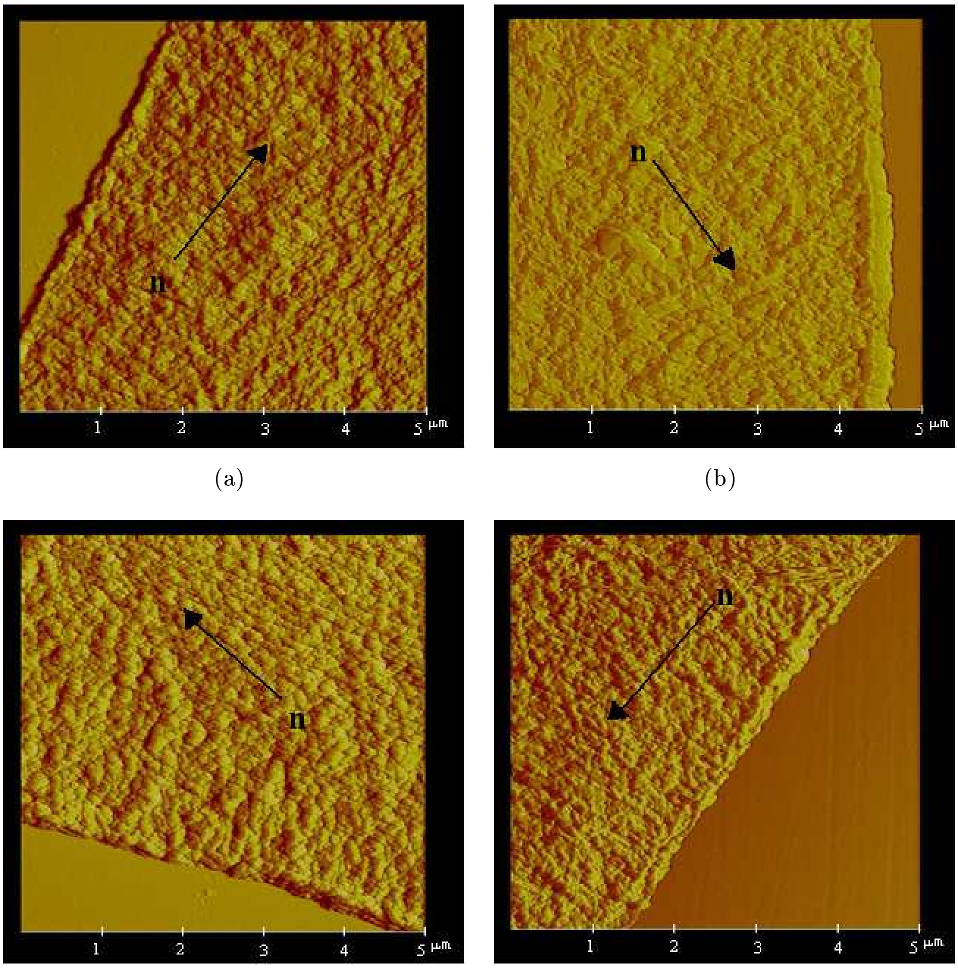

(a) (b)

(c) (d)

Figure 50: Here (a), (b), (c) and (d) correspond to positions 1, 2, 3 and 4 in Figure 49 respectively.

In Figure 50, the final stain of a laponite suspension droplet on hydrophobic glass has been scanned in the four different locations of Figure 49, with the scan size of 5×5 μm. It seems like the particles are arranged in a “circular” pattern, where the agglomerates chain up and point in the direction of the arrows.

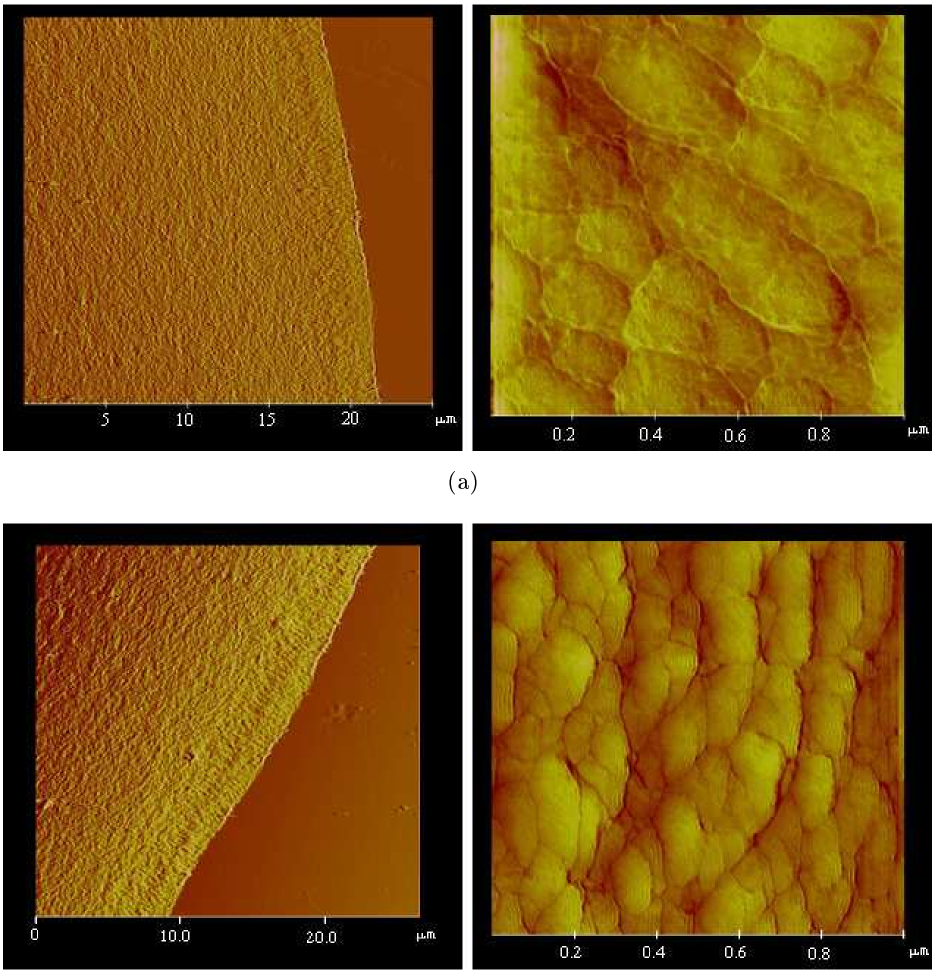

(a)

(b)

Figure 51: The pictures to the right are enlargements of the pictures to the left. (a) and (b) correspond to positions 2 and 4 in Figure 49 respectively.

The direction is, however, more evident in Figure 51, where the pictures to the right are enlargements of the pictures to the left, and is covering a 1×1 μm area. Here it is easier to see how the agglomerates have chained up, and how they are arranged in different directions.

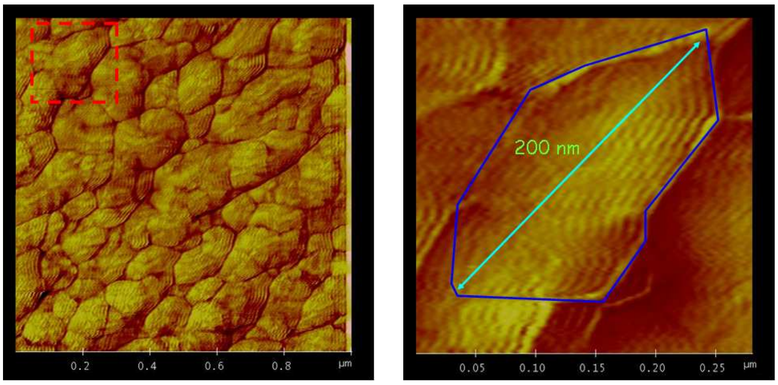

(a) (b)

Figure 52: Laponite agglomerates in a platelet-like organisation.

Figure 52(b) is an enlargement of the marked area in Figure 52(a). Here one can see how the clay is arranged in a platelet-like pattern, with the agglomerate length of about 200 nm.

It is evident from the pictures taken both through the optical microscope with the crossed polarisers and with the AFM, that there is some kind of nematic ordering in the foot of the evaporating suspension droplet and in the final stain. As was seen in Figure 52(b), the laponite clay is arranged in almost rod-like agglomerates, which is known to be the preferred shape of particles in a nematic phase.

As seen in Figure 53 there is no birefringence present in the 0.1% droplet. It is, however, very clear for the 0.2% and even more for the 0.5% droplet. There is also some birefringence in the 1.0% laponite droplet, but it is much weaker than for the others. The 0.1% laponite droplet has too little concentration of clay particles to be ordered. Both 0.2 and 0.5% obviously have enough, while it seems like 1.0% has a too high concentration, which leads to an early gelling and less movement by the particles. They are not able to settle down in a nematic pattern like for the less concentrated droplets.

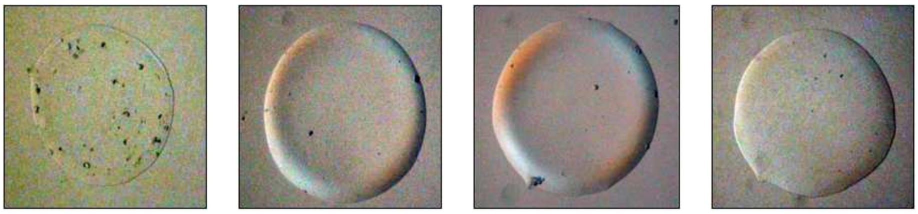

(a) (b) (c) (d)

Figure 53: Anisotropy versus Concentration for droplets deposited on hydrophobic glass. (a) 0.1% laponite, (b) 0.2% laponite, (c) 0.5% laponite and (d) 1.0% laponite.

10 Conclusion

For this Thesis the evaporation of suspension droplets on hydrophilic and hydrophobic substrates has been studied. The final conclusion from the experiments is that there are two key parameters in an evaporation process; the wetting properties of the substrate and the concentration of solute in the suspension.

The formation of the cap and foot is related to the wetting properties as could be seen in Section 9.1. The difference between the wetting and the non-wetting surfaces are obvious, as the droplet on hydrophilic surface is pinned in the moment it is deposited, while the droplet on hydrophobic glass is not pinned before the end of the evaporation process. It can also be seen how the cap and foot is totally separated for the hydrophilic glass, while they keep interacting for the hydrophobic. The wetting properties are also important in the formation of the nematic pattern in the foot of the evaporating droplet, as could be seen from the difference in residue anisotropy for the hydrophilic and hydrophobic surface.

The concentration of laponite in a suspension is crucial when it comes to both the formation of a foot and cap and a nematic pattern. As could be seen in Figure 53, the birefringence and nematic ordering was weak for high and low concentrations. It it also obvious that the separation of the droplet into a foot and a cap only is present for the 0.2 and 0.5% concentrations. This is especially evident in Figure 29 where the evolution of a 1% laponite suspension droplet on hydrophobic glass keeps the cap shape throughout the evaporation process, without separating into a cap and a foot.

For the experiments we assumed that the substrates used were clean, and that the hydrophobic glass was evenly silanised. In an open environment there will always be impurities on the glass surfaces, no matter how much they are cleaned. When the silanisation is carried out by hand, the surface can never be evenly hydrophobic either. We also assumed that the demineralised water was free from other particles, but the presence of particles may have been one of the reasons why some of the water droplets were pinned on hydrophilic glass.

The largest source of error is, however, the assumption that the droplets retained a circular shaped base throughout the evaporation process. This might have been true for some of the droplets, but most certainly not for most of them, and may have led to a large uncertainty in the calculation of the droplets' radius. As mentioned in Section 9, the measurement of the radius contains a large uncertainty due to the size of the droplets. They were too small and the pictures had a too low resolution using the SPIP for the radius to be calculated accurately enough. Another source of error is the number of samples used in the calculations, as all measurements had to be done manually.

As was emphasised in the Introduction, the theory for the relation between the radius and time is based on neglecting thermal and Marangoni effects. But these effects will always be present to a certain extent, and thus the theory is not completely correct.

For future research it would be desirable to investigate the laponite organisation further with the AFM. In that way it would be possible to find out if there really is a nematic organisation of the suspension particles throughout the rest of the stain. It would further be of interest to study the final deposits with small-angle X-ray scattering, SAXS, to see how the particles are arranged inside the edge. More experiments should also be carried out, to verify the results, and to work out a more accurate theory.

List of Figures

References

[1] Lars Ramstad Alme. Waxs studies of water transport in a layered synthetic silicate. Project Work, NTNU 2006.

[2] S. W. Bailey. Summary of recommendations of AIPEA nomenclature committee on clay minerals. *American Mineralogist*, 65:1–7, 1980.

[3] Eric Balnois, Serge Durand-Vidal, and Pierre Levitz. Probing the Morphology of Laponite Clay Colloids by Atomic Force Microscopy. *Langmuir*, 2003.

[4] David Baselt. *The tip-sample interaction in atomic force microscopy and its implications for biological applications.* PhD thesis, California Institute of Technology, 1993.

[5] F. Bergaya, B. K. G. Theng, and G. Lagaly, editors. *Handbook of Clay Science.* Elsevier, 2006.

[6] Ludwig Bergmann and Clemens Schaefer. *Optics of Waves and Particles.* Walter de Gruyter, 1999.

[7] Kaushik Bhattacharya. *Tip Shape and Resolution.* http://mechmat.caltech.edu/~kaushik/park/3-3-0.htm, California Institute of Technology, 2002.

[8] John Blackwell and Shane Thornton. *Mastering Optics.* McGraw-Hill Book Company, 1996.

[9] Max Born and Emil Wolf. *Principles of optics: Electromagnetic theory of propagation interference and diffraction of light.* Cambridge University Press, 2002.

[10] Thomas J. Bruno, Aneta Lewandowska, Faina Tsvetkov, Keith E. Miller, and Howard J.M. Hanley. Wall-coated open-tubular column chromatography on an organo-clay stationary phase. *Journal of Chromatography A*, pages 143–149, 2002.

[11] Light Microscopy Carl Zeiss. Stemi 2000, Stereomicroscopes. http://www.zeiss.de/C1256D18002CC306/0/59D7A3313047E51FC1256D5900335181/$file/46-0004_e.pdf.

[12] Carl Zeiss Mikroskopie. *Bedienungsanleitung, Stemi 1000/2000/2000C, Stereomikroskope*, 1998.

[13] Robert D. Deegan. Pattern formation in drying drops. *Physical Review E*, 61(1), 2000.

[14] Robert D. Deegan, Olgica Bakajin, Todd F. Dupont, Greg Huber, Sidney R. Nagel, and Thomas A. Witten. Capillary flow as the cause of ring stains from dried liquid drops. *Nature*, pages 827–830, 1997.

[15] Robert D. Deegan, Olgica Bakajin, Todd F. Dupont, Greg Huber, Sidney R. Nagel, and Thomas A. Witten. Contact line deposits in an evaporating drop. *Physical Review E*, 62(1), 2000.

[16] Digital Instruments Veeco Metrology Group. *MultiMode^{TM} SPM, Instruction Manual, Software Version 4.31ce*, 1996.

[17] Rajat Duggal, Fazle Hussain, and Matteo Pasquali. Self-Assembly of Single-Walled Carbon Nanotubes into Sheet by Drop Drying. *Advanced Materials*, 2006.

[18] J. O. Fossum, H. H. Bergene, Alex Hansen, B. O'Rourke, and G. Manificat. Self-affine crossover length in a layered silicate deposit. *Physical Review E*, 69(036108), 2004.

[19] Jon Otto Fossum. Physical phenomena in clays. *Physica A*, 270:270–277, 1999.

[20] Peter J. Haines. *Thermal Methods of Analysis - Principles, Applications and Problems*. Blackie Academic & Professional, 1995.

[21] M. D. Haw, M. Gillie, and W. C. K. Poon. Effects of Phase Behavior on the Drying of Colloidal Suspensions. *Langmuir*, 2002.

[22] Eugene Hecht. *Optics*. Addison-Wesley Publishing Company, 1987.

[23] Hua Hu and Ronald G. Larson. Marangoni Effect Reverses Coffee-Ring Depositions. *The Journal of Physical Chemistry B*, pages 7090–7094, 2006.

[24] Rolf E. Hummel. *Understanding Materials Science: History · Properties · Applications*. Springer, 2004.

[25] Rolf E. Hummel. *Electronic Properties of Materials*. Springer, 2005.

[26] HyperPhysics. Polarizers. http://hyperphysics.phy-astr.gsu.edu/hbase/phyopt/polcross.html.

[27] Amethyst Galleries Inc. The Clay Mineral Group. http://mineral.galleries.com/minerals/silicate/clays.htm, 1995.

[28] Mettler-Toledo International Inc. Thermogravimetric Analyzer (TGA). http://uk.mt.com/mt/products/products-applications_analytical-instruments_laboratory-thermal-analysis_thermal-analysis-modules/TGA_SDTA851e_Thermogravimetric_Analyzer_01623510810222521.jsp, 2007.

[29] SETARAM Instrumentation. Thermogravimetry (TGA). www.setaram.com/Thermogravimetry-TGA.htm.

[30] Hong-Qiang Li. AFM Resolution. http://www.chembio.uoguelph.ca/educmat/chm729/afm/resolution.htm, Department of Chemistry, University of Guelph, 1997.

[31] S. G. Lipson, H. Lipson, and D. S. Tannhauser. *Optical Physics*. Cambridge University Press, 1995.

[32] Jonathan Metcalf and Della Thompson, editors. *Illustrated Oxford Dictionary*. Dorling Kindersley & Oxford University Press, 2003.

[33] A. Mourchid, E. Lécolier, H. Van Damme, and P. Levitz. On Viscoelastic, Birefringent, and Swelling Properties of Laponite Clay Suspensions: Revisited Phase Diagram. *Langmuir*, pages 4718 – 4723, 1998.

[34] Pacific Nanotechnology. *Resolution in an atomic force microscope*. http://www.pacificnanotech.com/afm-tutorial_resolution-in-an-atomic-force-microscope.html, 2006.

[35] Van X. Nguyen and Kathleen J. Stebe. Patterning of Small Particles by a Surfactant-Enhanced Marangoni-Bénard Instability. *Physical Review Letters*, 2002.

[36] Jorge Nocedal and Stephen J. Wright. *Numerical Optimization*. Springer, 1999.

[37] F. Parisse and C. Allain. Drying of Colloidal Suspension Droplets: Experimental Study and Profile Renormalization. *Langmuir*, 1997.

[38] Kanak P. S. Parmar. *Oil dispersions of nanolayered silicates in an external electric field: An experimental study*. PhD thesis, NTNU, 2006.

[39] L. Pauchard and C. Allain. Stable and unstable surface evolution during the drying of a polymer solution drop. *Physical review E*, 2003.

[40] PixeLINK. *Megapixel FireWire Camera, User's Manual*, 2004.

[41] Emil J. Samuelsen. Materials physics: Structure, diffraction, imaging and spectroscopy, 2004.

[42] Noushine Shahidzadeh-Bonn, Salima Rafaï, Aza Azouni, and Daniel Bonn. Evaporating droplets. *Journal of Fluid Mechanics*, 2006.

[43] Leonid Shmuylovich, Amy Q. Shen, and Howard A. Stone. Surface Morphology of Drying Latex Films: Multiple Ring Formation. *Langmuir*, pages 3441–3445, 2002.

[44] F. G. Smith and J. H. Thomson. *Optics*. John Wiley & Sons Ltd., 1988.

[45] Gert Strobl. *Condensed Matter Physics: Crystals, Liquids, Liquid Crystals, and Polymers*. Springer, 2004.

[46] Eric Sultan, Arezki Boudaoud, and Martine Ben Amar. Evaporation of a thin film: diffusion of the vapour and marangoni instabilities. *Journal of Fluid Mechanics*, pages 183–202, 2005.

[47] Arizona State University The IN-VSEE Project. On the Relative Size of Things in Our Universe. http://invsee.asu.edu/Modules/size&scale/unit3/unit3.htm.

[48] Tom R. Thomas. *Rough Surfaces.* Imperial College Press, 1999.

[49] Van Nguyen Truskett and Kathleen J. Stebe. Influence of Surfactant on an Evaporating Drop: Fluorescence Images and Particle Deposition Patterns. *Langmuir*, 2003.

[50] N. Vandewalle, H. Monard, and J. G. McInerney. Physics of droplets, 2006. Proposal for a new COST Action, 165th CSO meeting 27-28 June 2006.

[51] Veeco. Metrology & Instrumentation : AFM / SPM, MultiMode. http://www.veeco.com/products/details.php?pid=177.

[52] Veeco Instruments Inc. *Scanning Probe Microscopy, Training Notebook, Software Version 3.0*, 2003.

[53] Veeco Probes. *Probes and Accessories*, 2006.

[54] B Velde. *CLAY MINERALS, A Physico-Chemical Explanation of their Occurence.* Elsevier, 1985.

[55] Wikipedia. Birefringence. http://en.wikipedia.org/wiki/Birefringence.

[56] Wikipedia. Microscope. http://en.wikipedia.org/wiki/Microscope.

[57] Wikipedia. Standard deviation. http://en.wikipedia.org/wiki/Standard_deviation.

[58] Wikipedia. *Atomic force microscope.* http://en.wikipedia.org/wiki/Atomic_force_microscope, 2006.

[59] Wikipedia. Clay. http://en.wikipedia.org/wiki/Clay, 2006.

[60] Wikipedia. Clay minerals. http://en.wikipedia.org/wiki/Clay_minerals, 2006.

[61] Jun Xu, Jianfeng Xia, Suck Won Hong, Zhiqun Lin, Feng Qiu, and Yuliang Yang. Self-Assembly of Gradient Concentric Rings via Solvent Evaporation from a Capillary Bridge. *Physical Review Letters*, 96(066104), 2006.

[62] A.L. Yarin, J.B. Szczech, C.M. Megaridis, J. Zhang, and D.R. Gamota. Lines of dense nanoparticle colloidal suspensions evaporating on a flat surface: Formation of non-uniform dried deposits. *Journal of Colloid and Interface Science*, pages 343–354, 2006.

A Nonlinear Least-Squares

Let $g(\boldsymbol{x}_i, \boldsymbol{\theta}) : \mathbb{R}^m \to \mathbb{R}$ be a nonlinear smooth function with respect to some model parameters $\boldsymbol{\theta} \in \mathbb{R}^k$ and the m dimensional vector $\boldsymbol{x}$. Further let y_i and $\boldsymbol{x}_i$, $i = 1, \ldots, n$, be a set of observed measurements, where we assume that $n > k$. The nonlinear least squares problem can then be written as:

$$\arg \min_{\boldsymbol{\theta}} \{f(\boldsymbol{\theta})\}, \tag{3}$$

where

$$f(\boldsymbol{\theta}) = \sum_{i=1}^{n} (y_i - g(\boldsymbol{x}_i, \boldsymbol{\theta}))^2$$

Due to the nonlinearity in the function above, this problem is in most cases a non-trivial task that requires some numerical solution such as the ones described in [36].

A.1 MATLAB Computer Code

```
Function that solves the non-linear least squares problem
min x sum((time/mass - myFun(x))^2)
            myFun = c*x^a

 INPUT :
  xlsFile  - An Excel file with x values in the first column
             and y values in the second column
  initial  - Vector with intitial values of x.
             x(1) = initial value of c
             x(2) = initial value of a

  saveFile- if given, the graph will be saved as an .eps file
             e.g 'philic1.eps'
 OUTPUT :
    c,a - see above

function [c, a] = lsquares(xlsFile,initial,saveFile)

data = xlsread(xlsFile);

x = data(:,1);
y = data(:,2);
n = length(x);
if(nargin ==1)
  initial = [0;0];
end

[res] = lsqnonlin(@(theta) myFun(theta,x(1:n),y(1:n)),initial);
```

```
c = res(1);
a = res(2);
plot(x,y,'b-',x,c*x.^a,'r--')

if(nargin==3)
  print(gcf,'-depsc2',saveFile)
end



function F = myFun(theta,t,y)
F = y -  theta(1) * x.^(theta(2));
```

B Standard deviation of a random variable

The standard deviation of a random variable X is defined as:

$$\sigma = \sqrt{\mathrm{E}((X - \mathrm{E}(X))^2)} = \sqrt{\mathrm{E}(X^2) - (\mathrm{E}(X))^2} \tag{4}$$

where $\mathrm{E}(X)$ is the expected value of X.

If X has the values $x_1, ..., x_N$ (real numbers), with each value of equal probability, then the standard deviation can be calculated as follows.

First the mean value of X, $\bar{x}$, is defined as the summation:

$$\bar{x} = \frac{1}{N} \sum_{1=1}^{N} x_i = \frac{x_1 + x_2 + \cdots + x_N}{N} \tag{5}$$

where N is the number of samples taken. Next, the standard deviation is simplified to:

$$\sigma = \sqrt{\frac{1}{N} \sum_{i=1}^{N} (x_i - \bar{x})^2} \tag{6}$$

[57].

C Laponite Data Sheet

ROCKWOOD ADDITIVES LIMITED / ROCKWOOD CLAY ADDITIVES GMBH

PRODUCT BULLETIN/Laponite®

WWW.LAPONITE.COM

Laponite RD

Description

Laponite RD is a synthetic layered silicate. It is insoluble in water but hydrates and swells to give clear and colourless colloidal dispersions. At concentrations of 2% or greater in water, highly thixotropic gels can be produced.

Application

Used for imparting a shear sensitive structure to a wide range of waterborne formulations. These include household and industrial surface coatings, cleansers, ceramic glazes, agrochemical, oilfield and horticultural products.

Typical Characteristics

Property	
Appearance	free flowing white powder
Bulk Density	1000 kg/m^3
Surface Area (BET)	370 m^2/g
pH (2% suspension)	9.8

Chemical Composition (dry basis)	
SiO_2	59.5%
MgO	27.5%
Li_2O	0.8%
Na_2O	2.8%
Loss on Ignition	8.2%

General Specifications

Property	Specification	Rockwood QA Test Code
Gel strength	22g min	ELP-L-1H
Sieve Analysis	2% Max >250 microns	ELP-L-6A
Free Moisture	10% Max	ELP-L-5A
Specifications can be agreed to meet individual requirements.		

Storage

Laponite products are hygroscopic and should be stored under dry conditions.

Southern Clay Products, Inc., Rockwood Additives Limited and Rockwood Clay Additives GmbH are wholly owned subsidiaries of Rockwood Specialties Group, Inc.

Rockwood Additives Limited
Moorfield Road Widnes
Cheshire UK WA8 3AA
Tel: +44 (0)151 495 2222 Fax: +44 (0)151 420 4401

Rockwood Clay Additives GmbH
Stadtwaldstr. 44
85368 Moosburg, Germany
Tel: +49 (0) 8761 72 150-0 Fax: +49 (0) 8761 72 150-334

Rockwood Specialties (Singapore) Pte. Limited
171 Chin Swee Road
Unit No: #10-08 San Centre Singapore 169877
Tel: +65 6532 0676 Fax: +65 6532 0502

Laponite Product Bulletin L-RD-06g

D Probes for the AFM

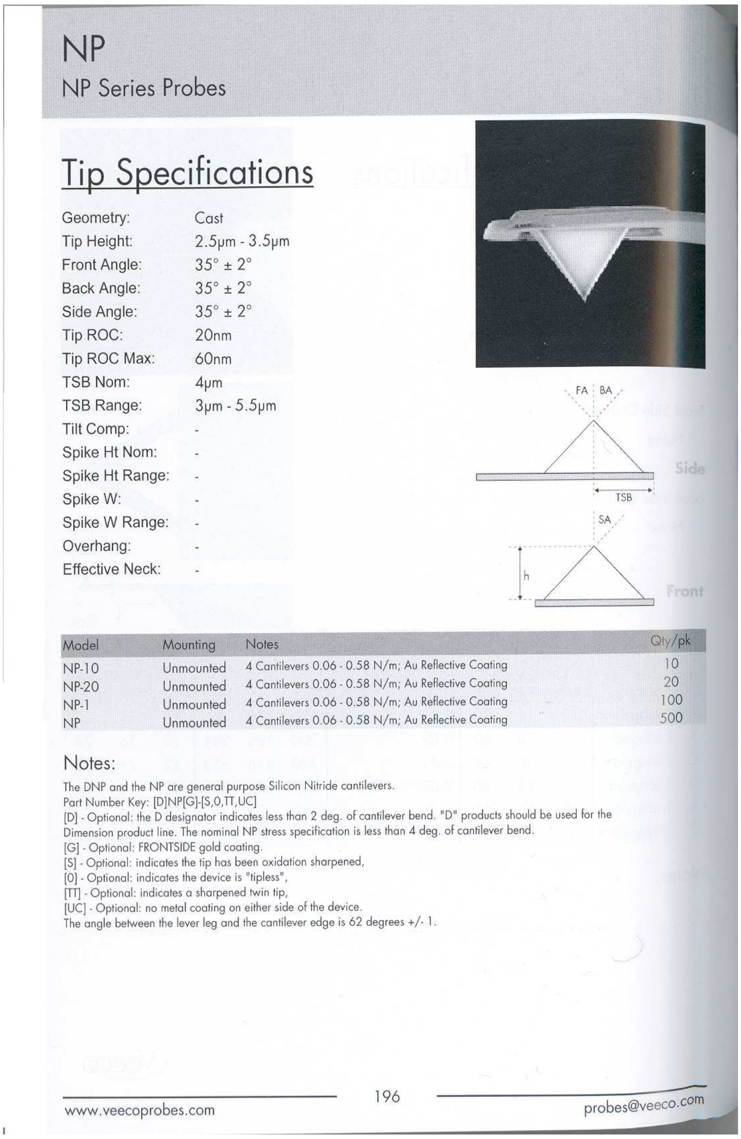

NP

NP Series Probes

Tip Specifications

Geometry:	Cast
Tip Height:	2.5μm - 3.5μm
Front Angle:	35° ± 2°
Back Angle:	35° ± 2°
Side Angle:	35° ± 2°
Tip ROC:	20nm
Tip ROC Max:	60nm
TSB Nom:	4μm
TSB Range:	3μm - 5.5μm
Tilt Comp:	-
Spike Ht Nom:	-
Spike Ht Range:	-
Spike W:	-
Spike W Range:	-
Overhang:	-
Effective Neck:	-

Model	Mounting	Notes	Qty/pk
NP-10	Unmounted	4 Cantilevers 0.06 - 0.58 N/m; Au Reflective Coating	10
NP-20	Unmounted	4 Cantilevers 0.06 - 0.58 N/m; Au Reflective Coating	20
NP-1	Unmounted	4 Cantilevers 0.06 - 0.58 N/m; Au Reflective Coating	100
NP	Unmounted	4 Cantilevers 0.06 - 0.58 N/m; Au Reflective Coating	500

Notes:

The DNP and the NP are general purpose Silicon Nitride cantilevers.
Part Number Key: [D]NP[G]-[S,0,TT,UC]
[D] - Optional: the D designator indicates less than 2 deg. of cantilever bend. "D" products should be used for the Dimension product line. The nominal NP stress specification is less than 4 deg. of cantilever bend.
[G] - Optional: FRONTSIDE gold coating.
[S] - Optional: indicates the tip has been oxidation sharpened,
[0] - Optional: indicates the device is "tipless",
[TT] - Optional: indicates a sharpened twin tip,
[UC] - Optional: no metal coating on either side of the device.
The angle between the lever leg and the cantilever edge is 62 degrees +/- 1.

www.veecoprobes.com 196 probes@veeco.com

Figure 54: Tip specifications for contact mode.

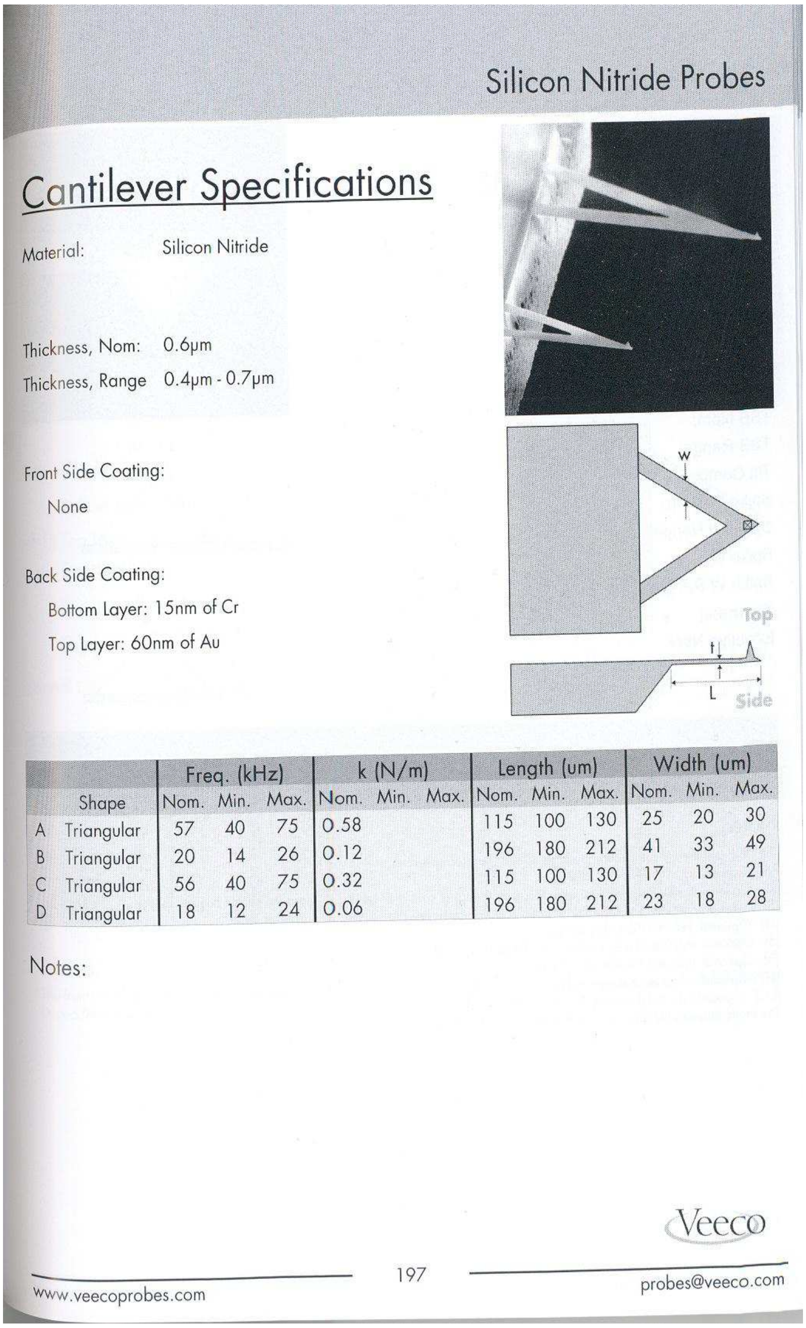

Silicon Nitride Probes

Cantilever Specifications

Material: Silicon Nitride

Thickness, Nom: 0.6μm

Thickness, Range 0.4μm - 0.7μm

Front Side Coating:

None

Back Side Coating:

Bottom Layer: 15nm of Cr

Top Layer: 60nm of Au

	Shape	Freq. (kHz)			k (N/m)			Length (um)			Width (um)		
		Nom.	Min.	Max.	Nom.	Min.	Max.	Nom.	Min.	Max.	Nom.	Min.	Max.
A	Triangular	57	40	75	0.58			115	100	130	25	20	30
B	Triangular	20	14	26	0.12			196	180	212	41	33	49
C	Triangular	56	40	75	0.32			115	100	130	17	13	21
D	Triangular	18	12	24	0.06			196	180	212	23	18	28

Notes:

www.veecoprobes.com 197 probes@veeco.com

Figure 55: Cantilever specifications for contact mode.